Article

Two-Stage Automatic Mass Balancing and Attitude Control for 3-DoF Spacecraft Attitude Simulators

Yong-Hwan Kim [1,*]

Space n Bean, 232 Gongneung-ro, Nowon-gu, Seoul 01811, Republic of Korea
* Correspondence: yongja2005@gmail.com

Abstract

Three-degree-of-freedom (3-DoF) air-bearing simulators are widely used for ground-based validation of spacecraft attitude determination and control systems. However, residual gravity torques caused by center-of-rotation to center-of-gravity (CR-CG) offsets can degrade simulation fidelity, particularly during coupled three-axis maneuvers. This paper presents a sequential coarse-to-fine automatic mass balancing framework, referred to as the Robust Automatic Mass Balancing Operator (RAMBO), designed to reduce residual CR-CG offsets under mechanical non-orthogonality and cross-axis coupling while maintaining a negative vertical offset for pendulum stability. The framework sequentially applies an active coarse stage (CRAMBO) for rapid offset reduction and a fine stage (FRAMBO) for precise CR-CG offset estimation using free-response motion data collected after platform reinitialization. To address the remaining offset-induced torque, a gravity-torque feedforward term is incorporated into a quaternion proportional-derivative (PD) controller. Hardware experiments during a coupled diagonal maneuver demonstrated that the estimated dynamic-equivalent CR-CG offset converged to approximately $[0.08, 0.12, -27.62]$ μm. Based on the onboard VN-100 estimates, the integrated balancing and control framework maintained steady-state attitude errors within $\pm 0.5^\circ$ and angular velocity errors within $\pm 0.4^\circ/\text{s}$ for roll and $\pm 0.2^\circ/\text{s}$ for pitch and yaw. A secondary IMU comparison further provided a roll/pitch consistency check rather than an independent ground-truth validation. These results demonstrate the effectiveness of the proposed approach for safety-constrained three-axis attitude-control validation.

Keywords: 3-DoF spacecraft attitude simulator; automatic mass balancing; CR-CG offset estimation; gravity torque compensation; least-squares estimation; non-orthogonal sliding mass mechanism

1. Introduction

Ground-based attitude simulators are widely used to verify spacecraft attitude determination and control systems (ADCS) prior to on-orbit operation [1–3]. Among them, three-degree-of-freedom (3-DoF) air-bearing simulators provide a nearly frictionless rotational environment, enabling hardware-in-the-loop (HIL) integration of sensors, actuators, and control algorithms [1,4–10]. Therefore, these simulators serve as experimental platforms for bridging the gap between numerical simulations and practical spacecraft attitude control validation. A key requirement for accurate ground-based attitude simulation is the alignment between the center of rotation (CR) and the center of gravity (CG) of the floating platform [8,9,11]. In a 1-g ground environment, a residual CR-CG offset generates a gravity-induced disturbance torque, which can distort the free rotational response of the simulator, reduce the available actuator margin, and degrade the reliability of attitude control experiments [12,13]. To mitigate this issue, manual balancing procedures and automatic mass balancing systems using sliding mass mechanisms have been investigated together with estimation algorithms, including least-squares estimation, recursive identification, and Kalman filter-based approaches [3,8,9,14–17]. Despite these efforts, practical hardware limitations remain challenging. Many mass balancing methods are formulated under idealized assumptions, such as orthogonal sliding mass axes, repeatable actuator

motion, and time-invariant mass properties [8,9]. However, non-orthogonal slider configurations can produce coupled relationships between slider displacements and centroid deviation components, indicating that the motion of one slider may affect multiple components of the CR-CG offset [18]. In actual experimental testbeds, similar coupling can also arise from geometric installation errors, assembly tolerances, actuator resolution limits, mechanical repeatability, sensor noise, and unmodeled residual disturbances [3,13]. These constraints indicate the need for a balancing strategy that can reduce residual offsets under non-ideal hardware conditions rather than relying on a single-stage or purely static calibration procedure. Another important design constraint is the vertical CR-CG offset. For spherical air-bearing simulators, the ideal zero-offset condition eliminates gravity-induced restoring torque; however, if the CG is located above the rotational center, the platform becomes prone to tipping, whereas a CG below the rotational center produces a pendulum-like restoring motion [11]. In the coordinate convention used in this study, this stable pendulum configuration corresponds to maintaining a slightly negative vertical CR-CG offset. Therefore, the balancing objective is not to force all components of the CR-CG offset to zero, but to reduce the residual gravity disturbance torque while preserving a negative vertical offset for safe platform operation. This remaining offset-induced torque should then be explicitly considered during attitude control experiments. To address these coupled challenges, this paper presents a two-stage automatic mass balancing system, referred to as the Robust Automatic Mass Balancing Operator (RAMBO), for a hemispherical 3-DoF spacecraft attitude simulator. The proposed RAMBO framework consists of a coarse balancing stage, CRAMBO, which rapidly reduces the initial CR-CG offset, and a fine balancing stage, FRAMBO, which refines the offset estimate through sequential platform reinitialization. This stop-and-restart operation is introduced to reduce the influence of transient dynamic disturbances during the fine estimation phase. To systematically address the remaining offset-induced torque, a gravity-torque feedforward compensation term derived from the final FRAMBO estimate, $\hat{\mathbf{r}}_{cg}$, is integrated into a baseline quaternion proportional-derivative (PD) controller [19,20]. The main contributions of this study are summarized as follows:

- A two-stage automatic mass balancing framework is proposed to reduce estimated residual CR-CG offsets under non-ideal sliding mass mechanisms, while maintaining a negative vertical-offset stability constraint.
- A batch least-squares-based CR-CG offset estimation procedure is integrated with sequential coarse-to-fine estimate-and-correct operation through CRAMBO and FRAMBO.
- A feedforward gravity-torque compensation law derived from the final estimated offset vector, $\hat{\mathbf{r}}_{cg}$, is incorporated into a quaternion PD attitude controller.
- The proposed balancing and control approach is experimentally validated using a Physik Instrumente (PI)-based 3-DoF spacecraft attitude simulator through a coupled three-axis diagonal maneuver.

The remainder of this paper is organized as follows. Section 2 describes the system configuration and dynamic model of the spacecraft attitude simulator. Section 3 presents the proposed two-stage automatic mass balancing system. Section 4 introduces the feedforward gravity-torque compensated attitude controller. Section 5 provides the numerical simulation and hardware validation results. Section 6 discusses practical limitations and applicability to ground-based ADCS validation. Finally, Section 7 concludes the paper.

2. System Configuration and Dynamic Modeling

This section presents the physical configuration and dynamic modeling of the developed three-degree-of-freedom (3-DoF) spacecraft attitude simulator. First, the hardware architecture of the air-bearing platform is introduced, including the attitude sensing, actuation, and automatic mass balancing subsystems. Then, the sliding mass mechanism and coordinate frames used in this study are defined. Based on these definitions, the gravity disturbance torque induced by the center-of-rotation to center-of-gravity (CR-CG) offset is formulated, and the rigid-body rotational dynamics with residual mass imbalance are derived.

2.1. Spacecraft Attitude Simulator Configuration

The experimental platform used in this study is a hemispherical air-bearing-based three-degree-of-freedom (3-DoF) spacecraft attitude simulator. The air bearing provides a nearly frictionless rotational environment about the bearing center [11], while the remaining gravity-induced disturbance torque is reduced through mass balancing. The platform allows unrestricted yaw rotation, whereas the roll and pitch motions are mechanically limited by the physical clearance of the hemispherical bearing and support structure. Therefore, all attitude control experiments in this study were conducted within the allowable angular motion range of the testbed. The simulator consists of four main subsystems: sensing, actuation, automatic mass balancing, and processing/communication. The sensing subsystem uses a VectorNAV VN-100 IMU/AHRS as the primary onboard attitude sensor for feedback control and performance evaluation. The VN-100 provides onboard attitude and angular-rate outputs based on its internal sensor-fusion algorithm; according to the manufacturer's product specifications, the nominal pitch/roll attitude accuracy is 0.5° RMS under static conditions and 1.0° RMS under dynamic conditions, with a typical gyroscope in-run bias stability of 5°/h [21]. In addition, a WITMotion BWT901CL IMU was installed as a secondary IMU and used only for roll/pitch relative-motion consistency checks. The actuation subsystem consists of three orthogonally mounted reaction wheel assemblies, each composed of a Maxon brushless DC motor, a motor driver, and a custom-fabricated wheel disk, and generates control torques for three-axis attitude maneuvers. The automatic mass balancing subsystem adjusts the center of gravity of the floating platform relative to the center of rotation using the RAMBO sliding mass mechanism. The processing and communication subsystem executes the balancing algorithm, attitude control law, actuator command generation, and experimental data logging. The overall configuration of the spacecraft attitude simulator is shown in Figure 1, and the electrical and communication interface is shown in Figure 2.

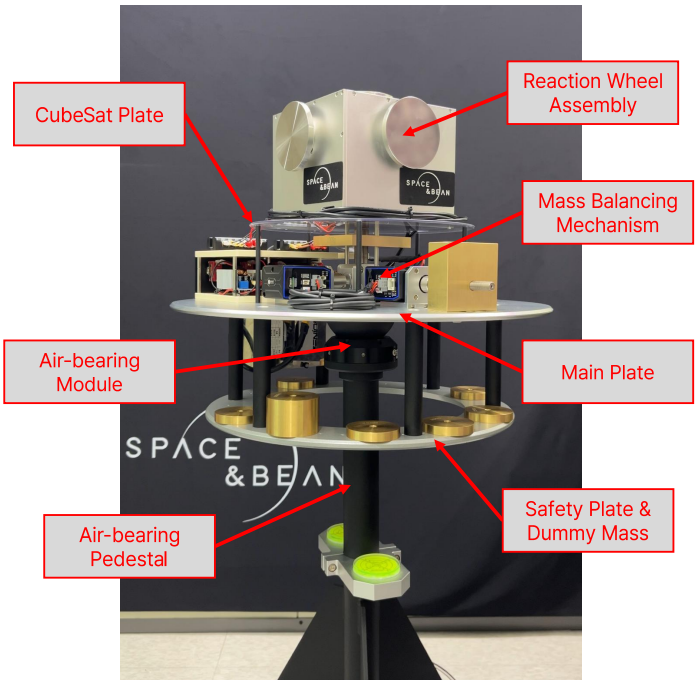

Figure 1. Overall configuration of the 3-DoF spacecraft attitude simulator.

The main physical and operational specifications of the simulator are summarized in Table 1, while the hardware components are listed in Table 2. Since the onboard components, reaction wheel assemblies, wiring, and sliding mass mechanisms are distributed over the floating platform, a residual center-of-rotation to center-of-gravity (CR-CG) offset inevitably remains after assembly. In addition, manual balancing is time-consuming and sensitive to small hardware changes, such as component replacement, cable routing, and initialization repeatability. These practical limitations motivate the use of an automatic mass balancing system, which is described in detail in Section 3.

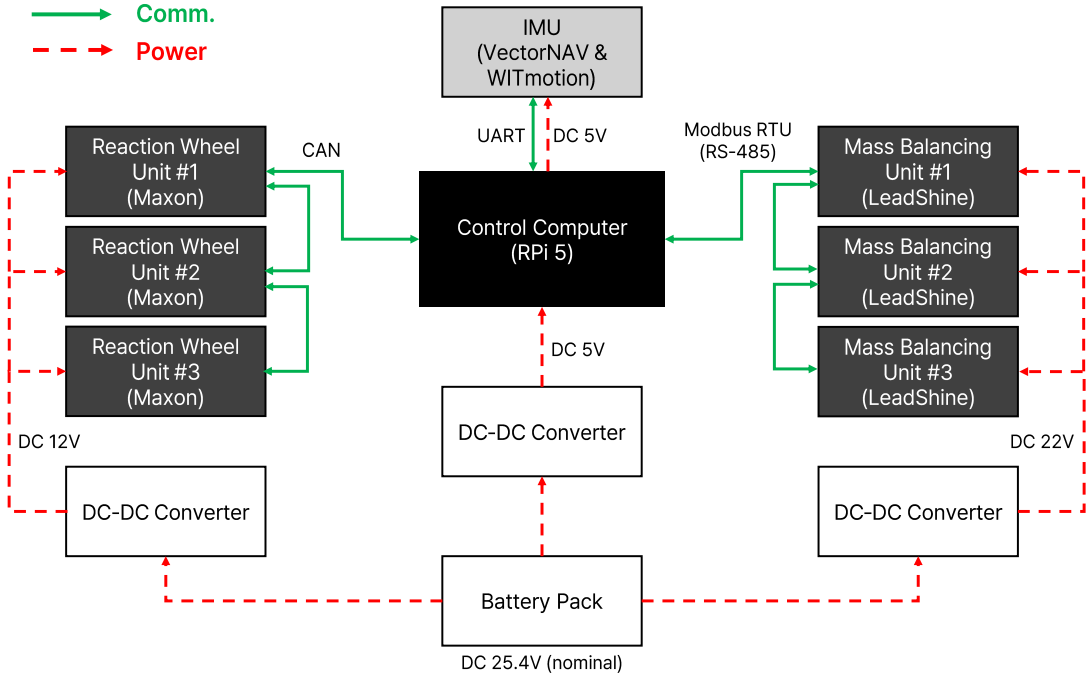

Figure 2. Electrical and communication interface of the 3-DoF spacecraft attitude simulator.

Table 1. Main physical and operational specifications of the 3-DoF spacecraft attitude simulator.

Category	Parameter	Value	Unit
Platform properties	Total floating mass, m_{tot}	26.95	kg
	Roll-axis MOI, J_{xx}	0.612	kg·m^2
	Pitch-axis MOI, J_{yy}	0.684	kg·m^2
	Yaw-axis MOI, J_{zz}	0.668	kg·m^2
	Allowable roll/pitch range	$\pm$30	deg
	Allowable yaw range	Unlimited	–
Air bearing	Sphere diameter	100	mm
	Operating pressure	80	psi
Reaction wheel assembly	Rated wheel speed	3000	RPM
	Maximum control torque	48.6	mN·m
	Angular momentum capacity	97.2	mN·m·s
Mass balancing mechanism	Sliding mass, m_x, m_y, m_z	1.5, 1.5, 1.0	kg
	Slider stroke, x and y axes	$\pm$32.5	mm
	Slider stroke, z axis	$\pm$23.0	mm
	Slider positioning resolution	5.0	µm

Note: The moments of inertia were estimated from the 3D CAD model of the simulator assembly.

Table 2. Main hardware components of the 3-DoF spacecraft attitude simulator.

Subsystem	Component	Manufacturer / Model	Description
Platform	Hemispherical air bearing	Physik Instrumente / A-653.045 [22]	Provides nearly frictionless rotational support
	Floating platform	In-house	Supports onboard sensors, actuators, and balancing mechanisms
Sensing	Primary IMU/AHRS	VectorNAV / VN-100 [21]	Provides onboard attitude and angular-rate feedback for control and evaluation
	Secondary IMU	WITmotion / BWT901CL [23]	Used for roll/pitch relative-motion consistency checks
Attitude control	BLDC motor	Maxon / EC-45 flat [24]	Drives each reaction wheel disk
	Motor driver	Maxon / EPOS Compact 50/5 [25]	Commands reaction wheel motor speed
	Motor encoder	Maxon / ENC MILE [26]	Provides wheel speed feedback for motor control
	Wheel disk	In-house	Provides rotational inertia for momentum exchange
Mass balancing	Stepper motor and encoder	Leadshine iCS-RS1706 [27]	Drives the sliding mass mechanism
	Sliding mass	In-house	Adjusts CR-CG offset along each balancing axis
Processing	Control computer	Raspberry Pi / 5	Executes RAMBO, attitude control, and data logging

2.2. Mass Balancing Mechanism and Coordinate Frames

The automatic mass balancing subsystem adjusts the center of gravity (CG) of the floating platform by translating three sliding masses along independently actuated axes. To describe the geometry of the mass balancing mechanism, two coordinate frames are defined. The inertial frame is denoted by $\mathcal{F}_N$, and the platform body-fixed frame is denoted by $\mathcal{F}_B$. The origin of $\mathcal{F}_B$ is located at the center of rotation (CR) of the hemispherical air bearing. Unless otherwise stated, all position vectors associated with the mass balancing mechanism are expressed in $\mathcal{F}_B$. Figure 3 shows the coordinate-frame and sliding-mass geometry definitions used in this study. Figure 4 shows the implemented mass balancing mechanism with three-axis sliding masses. The CR-CG offset vector is defined as

$$\mathbf{r}_{cg} = \begin{bmatrix} x_{cg} & y_{cg} & z_{cg} \end{bmatrix}^T, \tag{1}$$

where $\mathbf{r}_{cg}$ represents the position of the total platform CG with respect to the CR. The commanded stroke vector of the sliding masses is defined as

$$\mathbf{s} = \begin{bmatrix} s_x & s_y & s_z \end{bmatrix}^T, \tag{2}$$

where s_i denotes the commanded stroke of the i-th sliding mass from its reference position along the corresponding sliding-axis direction. Let m_0 and $\mathbf{r}_0$ denote the equivalent mass and CG position of the platform excluding the sliding masses. The position vector of the center of the i-th sliding mass is modeled as

$$\mathbf{p}_i(s_i) = \mathbf{p}_{i,0} + s_i \hat{\mathbf{u}}_{s_i}, \qquad i \in \{x, y, z\}, \tag{3}$$

where $\mathbf{p}_{i,0}$ is the reference position vector of the i-th sliding mass, and $\hat{\mathbf{u}}_{s_i}$ is the unit direction vector of the corresponding sliding axis expressed in $\mathcal{F}_B$. Therefore, the total CR-CG offset can be written as

$$\mathbf{r}_{cg}(\mathbf{s}) = \frac{m_0 \mathbf{r}_0 + \sum_{i \in \{x,y,z\}} m_i \mathbf{p}_i(s_i)}{m_{\text{tot}}}, \tag{4}$$

where m_i is the mass of each sliding mass and m_{tot} is the total floating mass of the simulator.

For an incremental change in the slider positions, the corresponding change in the CR-CG offset is expressed as

$$\Delta \mathbf{r}_{cg} = \frac{1}{m_{\text{tot}}} \mathbf{U}_s \mathbf{M}_s \Delta \mathbf{s}, \tag{5}$$

where

$$\mathbf{U}_s = \begin{bmatrix} \hat{\mathbf{u}}_{s_x} & \hat{\mathbf{u}}_{s_y} & \hat{\mathbf{u}}_{s_z} \end{bmatrix}, \qquad \mathbf{M}_s = \text{diag}(m_x, m_y, m_z). \tag{6}$$

In an ideal mass balancing mechanism, the sliding axes are perfectly aligned with the body-fixed axes, and thus $\mathbf{U}_s$ becomes the identity matrix. In the actual hardware, however, assembly tolerances and mechanical installation errors can make the sliding axes slightly non-orthogonal with respect to $\mathcal{F}_B$. As a result, the motion of a single sliding mass may affect multiple components of $\mathbf{r}_{cg}$, producing axis-to-axis coupling during the balancing process. This practical non-orthogonality motivates the two-stage balancing strategy introduced in Section 3.

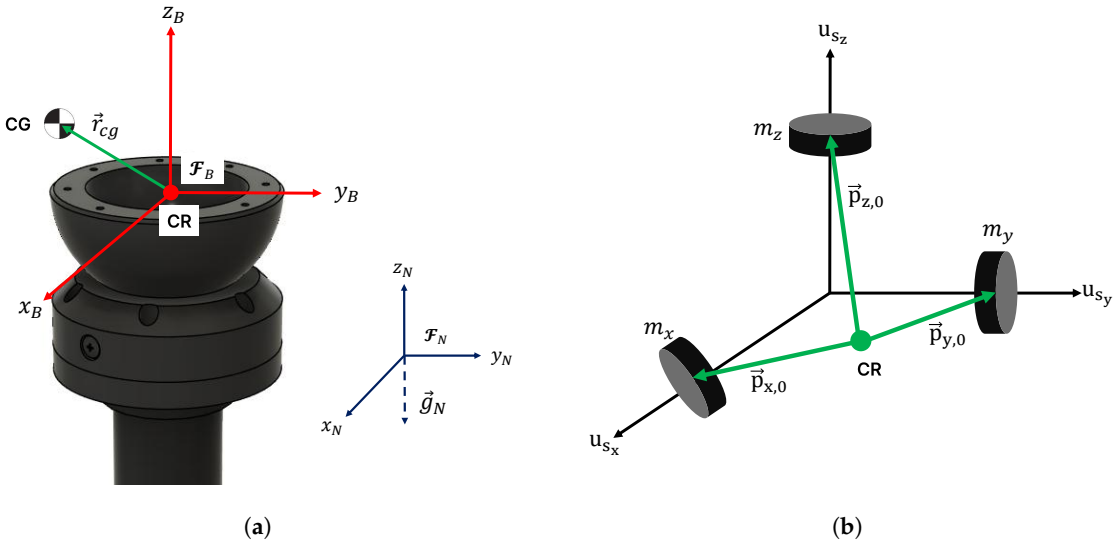

(**a**) (**b**)

Figure 3. Coordinate-frame and sliding-mass geometry definitions of the mass balancing system: (**a**) definition of the body-fixed frame $\mathcal{F}_B$, inertial frame $\mathcal{F}_N$, CR-CG offset vector, and gravity vector; (**b**) schematic definition of the sliding-mass reference positions and sliding-axis unit directions.

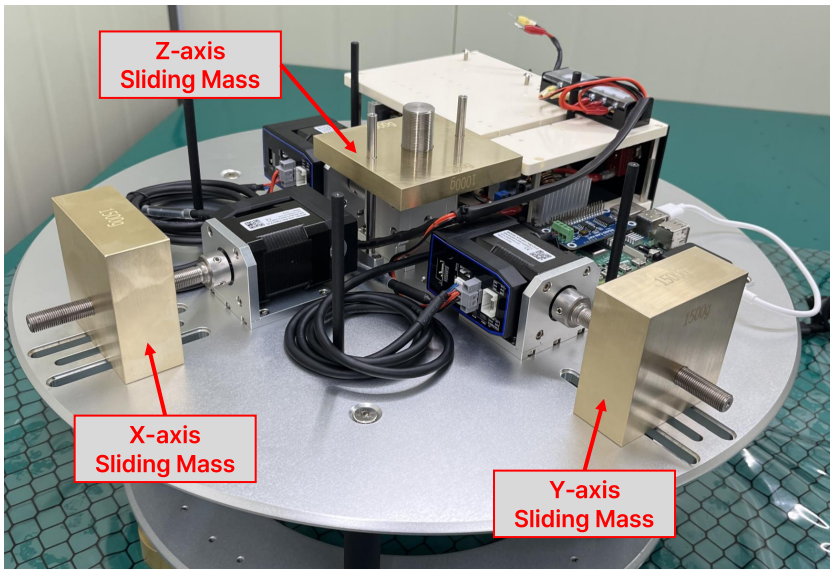

Figure 4. Implemented mass balancing mechanism with three-axis sliding masses.

2.3. CR-CG Offset and Gravity Disturbance Torque

In a 1-g ground environment, a residual offset between the center of rotation (CR) and the center of gravity (CG) generates a gravity-induced disturbance torque on the floating platform. Using the CR-CG offset vector $\mathbf{r}_{cg}$ defined in Section 2.2, the gravity disturbance torque expressed in the body-fixed frame $\mathcal{F}_B$ is written as

$$\boldsymbol{\tau}_g = \mathbf{r_{cg}}^{\times}(m_{\text{tot}}\mathbf{g}_B), \tag{7}$$

where m_{tot} is the total floating mass of the simulator, $\mathbf{g}_B$ is the gravity vector expressed in $\mathcal{F}_B$, and $\mathbf{r_{cg}}^{\times}$ denotes the skew-symmetric matrix of $\mathbf{r}_{cg}$, defined as

$$\mathbf{r_{cg}}^{\times} = \begin{bmatrix} 0 & -z_{cg} & y_{cg} \\ z_{cg} & 0 & -x_{cg} \\ -y_{cg} & x_{cg} & 0 \end{bmatrix}. \tag{8}$$

The gravity vector in the body-fixed frame is obtained by transforming the inertial gravity vector into $\mathcal{F}_B$ as

$$\mathbf{g}_B = \mathbf{C}_{BN}\mathbf{g}_N, \qquad \mathbf{g}_N = \begin{bmatrix} 0 & 0 & -g \end{bmatrix}^T, \tag{9}$$

where $\mathbf{C}_{BN}$ is the direction cosine matrix from the inertial frame $\mathcal{F}_N$ to the body-fixed frame $\mathcal{F}_B$, and g is the gravitational acceleration. When the CR and CG are perfectly aligned, $\mathbf{r}_{cg} = \mathbf{0}$ and the gravity disturbance torque vanishes. In practice, however, a small residual CR-CG offset remains because of sensor resolution, actuator positioning limits, mechanical assembly errors, and the stability requirement of the hemispherical air-bearing platform. For spherical air-bearing simulators, a CG located above the rotational center can make the platform prone to tipping, whereas a CG located below the rotational center produces a pendulum-like restoring motion [11]. In the coordinate convention used in this study, this stable pendulum configuration corresponds to maintaining a slightly negative vertical offset, $z_{cg} < 0$. To illustrate this design constraint, a simulation was conducted by varying only the vertical CR-CG offset while keeping the lateral offsets unchanged. As shown in Figure 5, the negative vertical offset produced a bounded oscillatory response, whereas the positive vertical offset led to an unstable tipping tendency.

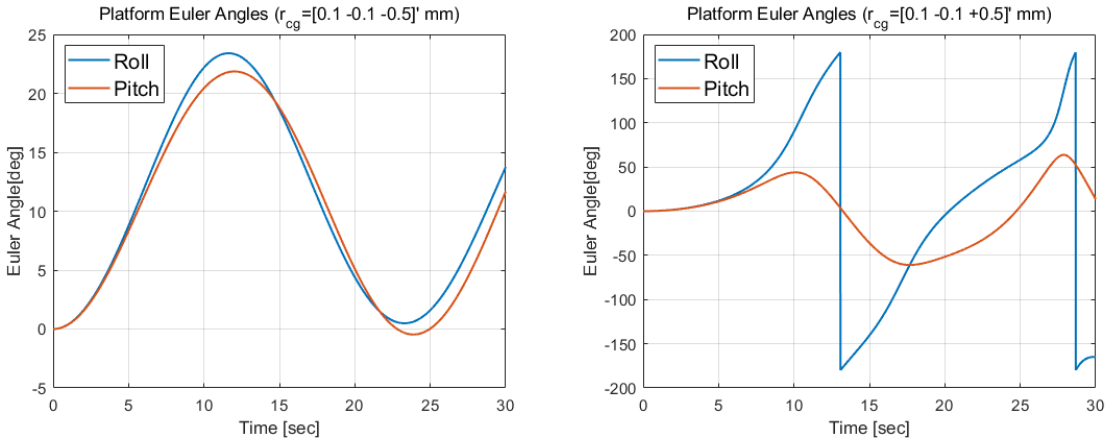

(**a**) (**b**)

Figure 5. Illustrative simulation of platform response under different vertical CR-CG offsets: (**a**) bounded oscillatory response for $z_{cg} = -0.5$ mm; (**b**) unstable tipping response for $z_{cg} = +0.5$ mm.

Therefore, the balancing objective is not to force all components of $\mathbf{r}_{cg}$ to zero, but to reduce the gravity disturbance torque while maintaining a negative vertical offset for safe platform operation. The magnitude of the gravity disturbance torque is directly related to both the residual CR-CG offset and the platform attitude. As the platform rotates, the gravity vector expressed in $\mathcal{F}_B$ changes through

$\mathbf{C}_{BN}$, and the resulting torque varies accordingly. This residual torque acts as a persistent disturbance during attitude control experiments and motivates the feedforward gravity-torque compensation strategy introduced in Section 4.

2.4. Rigid-Body Rotational Dynamics with Mass Imbalance

The floating platform is modeled as a rigid body rotating about the center of rotation (CR) of the hemispherical air bearing. Let $\boldsymbol{\omega} = [\omega_x\ \omega_y\ \omega_z]^T$ denote the angular velocity of the body-fixed frame $\mathcal{F}_B$ with respect to the inertial frame $\mathcal{F}_N$, expressed in $\mathcal{F}_B$. The inertia matrix of the floating platform is defined as

$$\mathbf{J} = \begin{bmatrix} J_{xx} & J_{xy} & J_{xz} \\ J_{yx} & J_{yy} & J_{yz} \\ J_{zx} & J_{zy} & J_{zz} \end{bmatrix}, \tag{10}$$

where the inertia properties of the floating platform were estimated from the 3D CAD model of the simulator assembly. Only the principal moments of inertia are summarized in Table 1, whereas the full inertia matrix was used in the attitude-control implementation.

Including the gravity disturbance torque caused by the residual CR-CG offset, the rotational dynamics of the platform can be written as

$$\mathbf{J}\dot{\boldsymbol{\omega}} + \boldsymbol{\omega}^{\times}\mathbf{J}\boldsymbol{\omega} = \boldsymbol{\tau}_c + \boldsymbol{\tau}_g + \boldsymbol{\tau}_d, \tag{11}$$

where $\boldsymbol{\tau}_c$ is the control torque applied to the platform by the reaction wheel assemblies, $\boldsymbol{\tau}_g$ is the gravity disturbance torque due to mass imbalance, and $\boldsymbol{\tau}_d$ represents unmodeled residual disturbances such as bearing friction, cable effects, actuator imperfections, and measurement-induced uncertainties. The skew-symmetric matrix $\boldsymbol{\omega}^{\times}$ is defined as

$$\boldsymbol{\omega}^{\times} = \begin{bmatrix} 0 & -\omega_z & \omega_y \\ \omega_z & 0 & -\omega_x \\ -\omega_y & \omega_x & 0 \end{bmatrix}. \tag{12}$$

The gravity disturbance torque $\boldsymbol{\tau}_g$ is given by the CR-CG offset model derived in Section 2.3. Therefore, when the CR and CG are perfectly aligned, $\mathbf{r}_{cg} = \mathbf{0}$ and the gravity disturbance torque is eliminated. In the actual testbed, however, a residual CR-CG offset remains after mass balancing, and the corresponding gravity disturbance torque acts as a persistent external torque during attitude control experiments.

For controller design and simulation, the angular acceleration can be expressed as

$$\dot{\boldsymbol{\omega}} = \mathbf{J}^{-1}\left(\boldsymbol{\tau}_c + \boldsymbol{\tau}_g + \boldsymbol{\tau}_d - \boldsymbol{\omega}^{\times}\mathbf{J}\boldsymbol{\omega}\right). \tag{13}$$

This model provides the dynamic basis for the feedforward gravity-torque compensation strategy introduced in Section 4.

3. Two-Stage Automatic Mass Balancing System

This section presents the proposed two-stage automatic mass balancing system, referred to as the Robust Automatic Mass Balancing Operator (RAMBO). The objective of RAMBO is to estimate the residual CR-CG offset of the floating platform and command the mass balancing mechanism to reduce the gravity disturbance torque. The proposed system combines batch least-squares-based offset estimation, decision logic for slider command generation, and sequential coarse-to-fine balancing operation. The coarse stage, CRAMBO, rapidly reduces the initial offset, whereas the fine stage, FRAMBO, refines the remaining offset under reduced residual-disturbance conditions.

3.1. Overview of RAMBO

The Robust Automatic Mass Balancing Operator (RAMBO) is designed as a pre-test/intermittent mass-balancing framework for reducing the residual CR-CG offset of the floating platform before attitude-control experiments, rather than as a continuous online mass redistribution scheme during closed-loop attitude control. Rather than a single estimation algorithm, RAMBO is formulated as a sequential coarse-to-fine balancing framework that combines free-response data processing, batch least-squares-based CR-CG offset estimation, decision logic for slider command generation, and stage-dependent operation of the mass balancing mechanism. The overall architecture of RAMBO is shown in Figure 6. During each balancing execution, RAMBO receives the measured attitude quaternion, $\mathbf{q}$, and angular velocity, $\boldsymbol{\omega}$, obtained during a free-response interval. These data are used to estimate the residual CR-CG offset, $\hat{\mathbf{r}}_{cg}$, and to determine whether the current balancing requirement is satisfied. If additional correction is required, RAMBO computes the commanded slider displacement, $\Delta\mathbf{s}_{cmd}$, which is sent to the mass balancing mechanism. The resulting actual slider displacement is denoted by $\Delta\mathbf{s}_{act}$. RAMBO is operated in two sequential stages. The first stage, Coarse RAMBO (CRAMBO), rapidly reduces the initial CR-CG offset through an automatic iterative balancing loop. Once the coarse balancing requirement is satisfied, the system proceeds to the second stage, Fine RAMBO (FRAMBO), which refines the remaining offset using smaller correction commands and platform reinitialization between balancing trials. This stop-and-restart operation is introduced to reduce the influence of residual transient disturbances and improve the reliability of fine offset estimation. The final output of RAMBO is the refined CR-CG offset estimate obtained after the FRAMBO stage, which is then held fixed during the subsequent attitude-control maneuver. This final estimate is used not only to determine the balanced condition of the platform but also to construct the feedforward gravity-torque compensation term in the attitude controller, as described in Section 4. The detailed batch least-squares estimation procedure used inside RAMBO is presented in the following subsection.

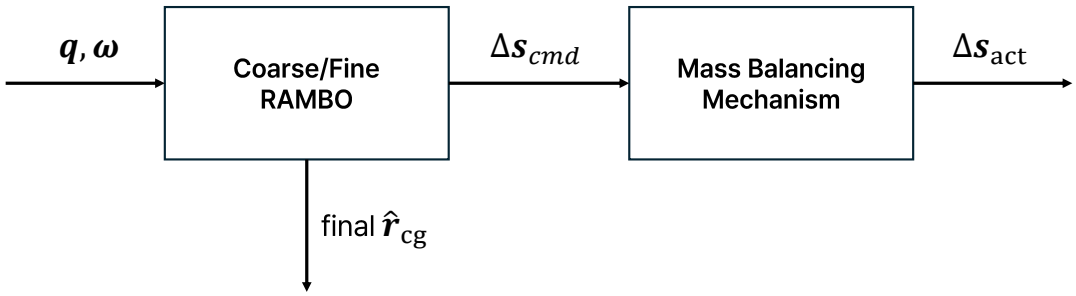

Figure 6. Overall architecture of the Robust Automatic Mass Balancing Operator (RAMBO).

3.2. Batch Least-Squares-Based CR-CG Offset Estimation

The CR-CG offset estimation procedure follows the integrated least-squares-based balancing approach reported in [2,12], with modifications for the proposed RAMBO operation. During the estimation interval, the platform is released under a free-response condition without reaction wheel control torque. The measured attitude quaternion and angular velocity data are then used to estimate the residual CR-CG offset of the floating platform. For the estimation model, a simplified low-rate free-response approximation is used. In this approximation, products-of-inertia effects, gyroscopic coupling terms, and residual disturbance torques are not explicitly identified and are treated as part of

the estimation residual. Under this approximation, the gravity-torque-dominant rotational response can be written as

$$\dot{\boldsymbol{\omega}} = \begin{bmatrix} \frac{m_{\text{tot}} g}{J_{xx}} \left(-y_{cg} \cos\phi \cos\theta + z_{cg} \sin\phi \cos\theta\right) \\ \frac{m_{\text{tot}} g}{J_{yy}} \left(x_{cg} \cos\phi \cos\theta + z_{cg} \sin\theta\right) \\ \frac{m_{\text{tot}} g}{J_{zz}} \left(-x_{cg} \sin\phi \cos\theta - y_{cg} \sin\theta\right) \end{bmatrix}, \tag{14}$$

where ϕ and θ denote the roll and pitch angles reconstructed from the measured attitude quaternion, respectively. This simplified model is used only for CR-CG offset estimation inside RAMBO, whereas the full inertia matrix is used in the attitude-control implementation. Integrating the above equation over a short time interval from t_k to t_{k+1} gives

$$\Delta\boldsymbol{\omega}_k = \boldsymbol{\Phi}_k \mathbf{r}_{cg}, \tag{15}$$

where

$$\Delta\boldsymbol{\omega}_k = \begin{bmatrix} \omega_{x,k+1} - \omega_{x,k} \\ \omega_{y,k+1} - \omega_{y,k} \\ \omega_{z,k+1} - \omega_{z,k} \end{bmatrix}, \qquad \mathbf{r}_{cg} = \begin{bmatrix} x_{cg} & y_{cg} & z_{cg} \end{bmatrix}^T. \tag{16}$$

Assuming that ϕ and θ remain approximately constant within the short interval, the regression matrix for the k-th interval is obtained using trapezoidal integration as

$$\boldsymbol{\Phi}_k = \begin{bmatrix} 0 & \Phi_{12,k} & \Phi_{13,k} \\ \Phi_{21,k} & 0 & \Phi_{23,k} \\ \Phi_{31,k} & \Phi_{32,k} & 0 \end{bmatrix}, \tag{17}$$

with

$$\Phi_{12,k} = -\frac{m_{\text{tot}} g \Delta t}{2 J_{xx}} [(\cos\phi \cos\theta)_{k+1} + (\cos\phi \cos\theta)_k], \tag{18}$$

$$\Phi_{13,k} = \frac{m_{\text{tot}} g \Delta t}{2 J_{xx}} [(\sin\phi \cos\theta)_{k+1} + (\sin\phi \cos\theta)_k], \tag{19}$$

$$\Phi_{21,k} = \frac{m_{\text{tot}} g \Delta t}{2 J_{yy}} [(\cos\phi \cos\theta)_{k+1} + (\cos\phi \cos\theta)_k], \tag{20}$$

$$\Phi_{23,k} = \frac{m_{\text{tot}} g \Delta t}{2 J_{yy}} [(\sin\theta)_{k+1} + (\sin\theta)_k], \tag{21}$$

$$\Phi_{31,k} = -\frac{m_{\text{tot}} g \Delta t}{2 J_{zz}} [(\sin\phi \cos\theta)_{k+1} + (\sin\phi \cos\theta)_k], \tag{22}$$

$$\Phi_{32,k} = -\frac{m_{\text{tot}} g \Delta t}{2 J_{zz}} [(\sin\theta)_{k+1} + (\sin\theta)_k], \tag{23}$$

where $\Delta t = t_{k+1} - t_k$ is the sampling interval. By stacking the data over the estimation window, the batch regression equation is written as

$$\Delta\boldsymbol{\Omega}_L = \boldsymbol{\Phi}_L \mathbf{r}_{cg}, \tag{24}$$

where

$$\Delta\boldsymbol{\Omega}_L = \begin{bmatrix} \Delta\boldsymbol{\omega}_1 \\ \Delta\boldsymbol{\omega}_2 \\ \vdots \\ \Delta\boldsymbol{\omega}_N \end{bmatrix}, \qquad \boldsymbol{\Phi}_L = \begin{bmatrix} \boldsymbol{\Phi}_1 \\ \boldsymbol{\Phi}_2 \\ \vdots \\ \boldsymbol{\Phi}_N \end{bmatrix}. \tag{25}$$

The CR-CG offset estimate is then obtained using the batch least-squares solution:

$$\hat{\mathbf{r}}_{cg} = \left(\boldsymbol{\Phi}_L^T \boldsymbol{\Phi}_L\right)^{-1} \boldsymbol{\Phi}_L^T \Delta\boldsymbol{\Omega}_L. \tag{26}$$

The estimate $\hat{\mathbf{r}}_{cg}$ obtained from Eq. (26) should be interpreted as a dynamic-equivalent CR-CG offset identified from the free-response motion, rather than as an independently measured physical location of the center of gravity. The batch least-squares estimator determines the offset vector that best explains the measured attitude and angular-rate histories under the simplified estimation model. Therefore, $\hat{\mathbf{r}}_{cg}$ may include the effects of sensor noise, bias drift, unmodeled disturbance torques, and modeling approximations within the selected estimation window. In this study, this estimate is used as a model-consistent residual imbalance parameter for slider correction and gravity-torque feedforward compensation. Figure 7 summarizes the data processing, batch least-squares estimation, and decision logic used inside RAMBO. In the present implementation, the raw slider correction is generated using a nominal diagonal mass-shift relation, in which each sliding mass is assumed to primarily affect the corresponding CR-CG offset component. This command generation does not require explicit identification of the full non-orthogonal slider-axis matrix, $\mathbf{U}_s$. Instead, residual cross-axis coupling and command errors are mitigated through repeated estimate-and-correct operation and stage-dependent weighting in CRAMBO and FRAMBO. Using this dynamic-equivalent offset estimate, $\hat{\mathbf{r}}_{cg}$, the raw slider correction is computed as

$$\Delta s_{\mathrm{raw},i} = \left(\hat{r}_{cg,\mathrm{tar},i} - \hat{r}_{cg,i}\right)\frac{m_{\mathrm{tot}}}{m_i}, \qquad i \in \{x, y, z\}. \tag{27}$$

After $\Delta\mathbf{s}_{\mathrm{raw}}$ is obtained, the final slider command, $\Delta\mathbf{s}_{\mathrm{cmd}}$, is determined through the stage-dependent decision logic and weighting rules. The detailed procedures for computing $\Delta\mathbf{s}_{\mathrm{cmd}}$ in CRAMBO and FRAMBO are described in Sections 3.3 and 3.4, respectively.

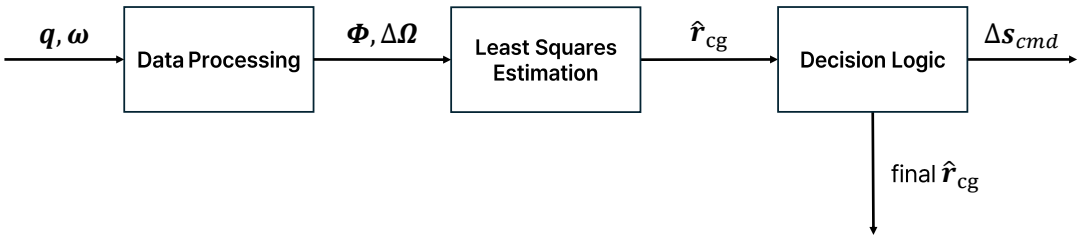

Figure 7. Batch least-squares CR-CG offset estimation and decision logic in RAMBO.

3.3. Coarse Balancing Stage: CRAMBO

Coarse RAMBO (CRAMBO) is the first stage of the proposed two-stage automatic mass balancing system. The objective of CRAMBO is to rapidly reduce the initial CR-CG offset to a coarse admissible range before applying the fine balancing stage. CRAMBO is operated as an automatic iterative loop consisting of free-response data processing, least-squares-based offset estimation, requirement checking, and slider command execution. At the beginning of each CRAMBO iteration, the platform is released under a free-response condition, and the attitude and angular velocity data are collected over the prescribed CRAMBO estimation window, $t_{\mathrm{C,win}}$. The measured data are processed using the batch least-squares procedure described in Section 3.2, yielding the current CR-CG offset estimate, $\hat{\mathbf{r}}_{cg}$. The CRAMBO decision logic first evaluates whether the estimated lateral offset components satisfy the coarse lateral balancing requirement:

$$|\hat{x}_{cg}| \le \alpha_C \quad \text{and} \quad |\hat{y}_{cg}| \le \alpha_C, \tag{28}$$

where α_C is the allowable coarse lateral offset bound. The vertical offset is then evaluated using the coarse admissible range:

$$\beta_{C,l} \le \hat{z}_{cg} \le \beta_{C,u}, \tag{29}$$

where $\beta_{C,l}$ and $\beta_{C,u}$ define the lower and upper bounds of the allowable vertical offset range. The vertical range is selected in the negative direction to maintain a pendulum-like restoring tendency during coarse balancing. If the lateral offset requirement is not satisfied, CRAMBO computes the lateral slider command components, $\Delta s_{cmd,x}$ and $\Delta s_{cmd,y}$. Depending on the vertical offset condition, a weighting factor $w_{C,\alpha}$ may be applied to the lateral correction command to avoid excessive correction when the vertical offset is outside the coarse admissible range. Similarly, if the vertical offset does not satisfy the prescribed range, the vertical slider command component, $\Delta s_{\mathrm{cmd},z}$, is determined from the raw correction using the CRAMBO decision logic. In this process, one of the weighting factors $w_{C,\beta,1}$, $w_{C,\beta,2}$, and $w_{C,\beta,3}$ may be applied depending on the estimated vertical offset. These weighting factors make the coarse correction conservative and reduce the risk of overcorrection caused by unmodeled cross-axis coupling and actuator repeatability errors. Figure 8 shows the operational flowchart of the CRAMBO stage. The procedure is repeated until both the lateral and vertical coarse balancing requirements are satisfied. The main role of CRAMBO is not to achieve the final balancing accuracy, but to bring the platform into a stable and sufficiently balanced condition for the subsequent FRAMBO stage. The remaining residual offset after CRAMBO is further refined by FRAMBO, as described in Section 3.4.

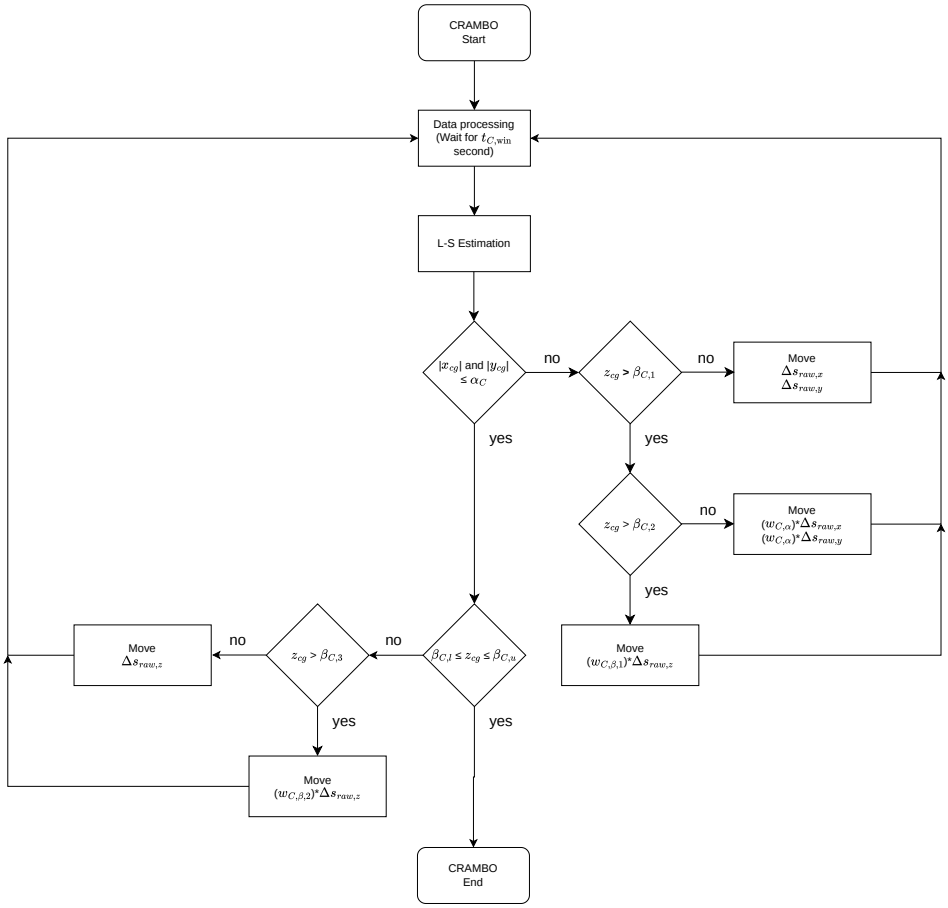

Figure 8. Operational flowchart of the Coarse RAMBO (CRAMBO) stage.

3.4. Fine Balancing Stage: FRAMBO

Fine RAMBO (FRAMBO) is the second stage of the proposed two-stage automatic mass balancing system. After CRAMBO reduces the initial CR-CG offset to a coarse admissible range, FRAMBO refines the remaining offset under reduced disturbance conditions. Unlike CRAMBO, FRAMBO is executed as a single fine balancing action rather than a fully automatic continuous loop. After each FRAMBO execution, the platform is stopped and reinitialized before the next free-response estimation trial. At

the beginning of each FRAMBO execution, the platform is released under a free-response condition, and the attitude and angular velocity data are collected over the prescribed FRAMBO estimation window, $t_{\mathrm{F,win}}$. The measured data are processed using the batch least-squares estimator described in Section 3.2, yielding the current CR-CG offset estimate, $\hat{\mathbf{r}}_{cg}$. The FRAMBO decision logic first evaluates whether the estimated lateral offset components satisfy the fine lateral balancing requirement:

$$|\hat{x}_{cg}| \leq \alpha_F \quad \text{and} \quad |\hat{y}_{cg}| \leq \alpha_F, \tag{30}$$

where α_F is the allowable fine lateral offset bound. The vertical offset is then evaluated using the fine admissible range:

$$\beta_{F,l} \leq \hat{z}_{cg} \leq \beta_{F,u}, \tag{31}$$

where $\beta_{F,l}$ and $\beta_{F,u}$ define the lower and upper bounds of the desired vertical offset range. This range is selected to remain negative so that the platform maintains passive pendulum-like stability while reducing the residual gravity disturbance torque. If the fine balancing requirement is not satisfied, FRAMBO generates the commanded slider displacement, $\Delta\mathbf{s}_{cmd}$, according to the estimated offset condition. Compared with CRAMBO, FRAMBO applies smaller and condition-dependent correction commands to reduce the risk of overcorrection. In particular, intermediate vertical thresholds, $\beta_{F,1}$ through $\beta_{F,5}$, are used to determine whether the lateral correction, vertical correction, or weighted correction should be applied. The weighting factors $w_{F,\alpha}$ and $w_{F,\beta,1}, \ldots, w_{F,\beta,4}$ are introduced to limit the correction magnitude when the estimated offset approaches the fine admissible negative vertical-offset range. This conservative correction strategy reduces overshoot and mitigates the effect of residual cross-axis coupling that is not explicitly captured by the nominal slider-command model. Figure 9 shows the operational flowchart of the FRAMBO stage. Each FRAMBO execution terminates after the corresponding slider command is applied. The platform is then brought to rest and reinitialized before the next estimation trial. This stop-and-restart operation reduces the influence of transient motion, residual oscillation, and axis-to-axis coupling during fine offset estimation. The final offset estimate obtained after FRAMBO is used as the balanced CR-CG condition of the platform and is held fixed during the subsequent attitude-control maneuver. This estimate is also used to construct the feedforward gravity-torque compensation term in the attitude controller, as described in Section 4.

3.5. Summary of RAMBO Operational Logic

The overall RAMBO operation is summarized as a sequential coarse-to-fine mass balancing procedure. Both CRAMBO and FRAMBO use the same batch least-squares-based CR-CG offset estimator described in Section 3.2, but they differ in their operational purpose, execution mode, correction magnitude, and stopping condition. CRAMBO rapidly reduces the initial offset through an automatic iterative loop, whereas FRAMBO refines the remaining offset through single-step executions with platform stop-and-restart operation. Table 3 summarizes the key operational differences between CRAMBO and FRAMBO.

Table 3. Key operational differences between CRAMBO and FRAMBO.

Item	CRAMBO	FRAMBO
Purpose	Rapid coarse reduction of the initial CR-CG offset	Fine refinement of the residual CR-CG offset
Execution mode	Automatic iterative loop	Single-step execution with platform stop-and-restart operation
Correction strategy	Relatively large correction using coarse bounds	Reduced and condition-dependent correction to avoid overcorrection
Final role	Provides a coarse admissible initial condition for FRAMBO	Provides the final offset estimate for gravity-torque compensation

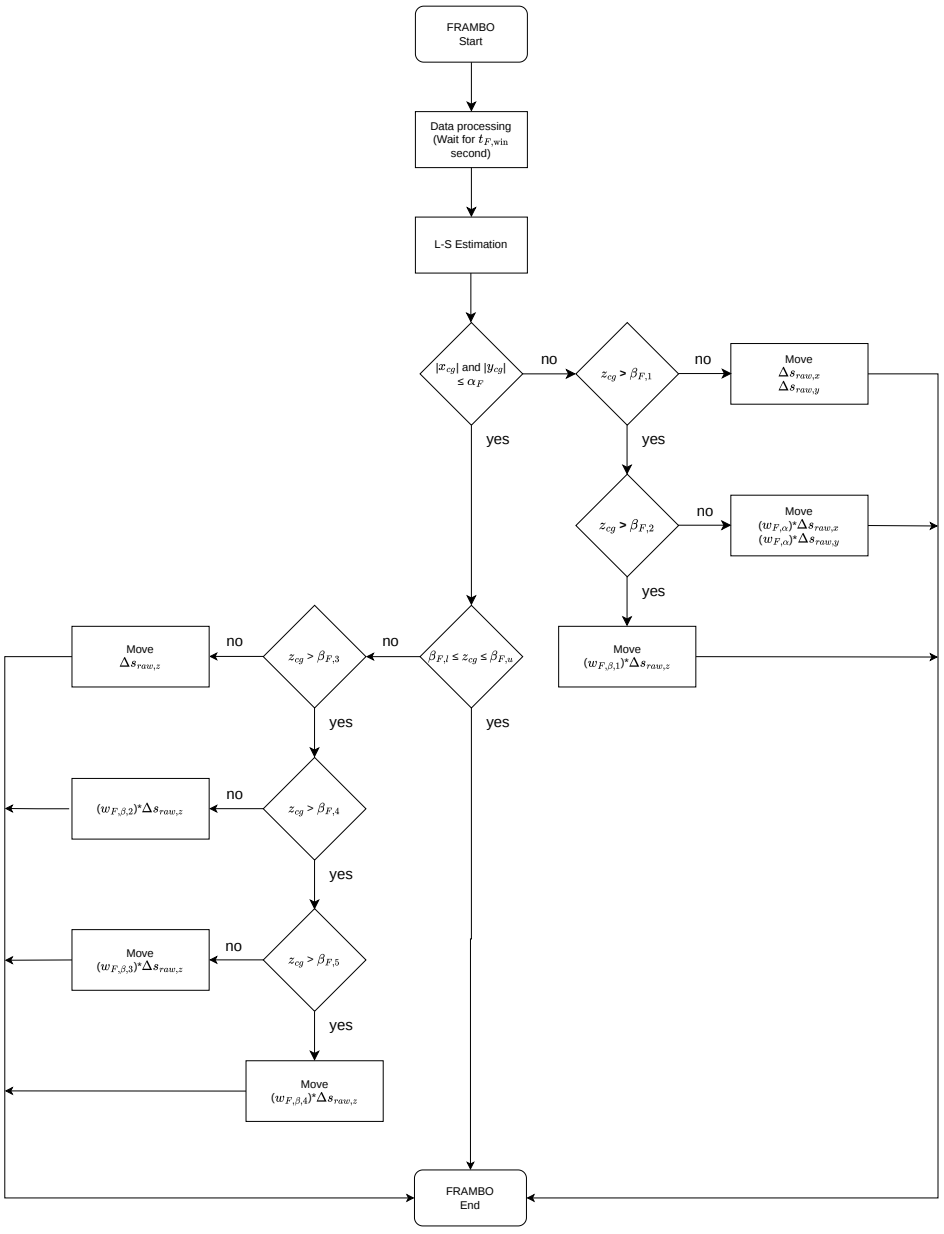

Figure 9. Operational flowchart of the Fine RAMBO (FRAMBO) stage.

After the FRAMBO stage, the final estimated offset vector, $\hat{\mathbf{r}}_{cg}$, is stored as the balanced CR-CG condition of the platform and held fixed during the subsequent attitude-control maneuver. This value is subsequently used to construct the feedforward gravity-torque compensation term, as described in Section 4.

4. Gravity-Compensated Attitude Control

Although the RAMBO procedure reduces the CR-CG offset of the floating platform, a small residual offset remains because of hardware resolution, sensing uncertainty, and the stability requirement of the hemispherical air-bearing platform. This residual offset generates a gravity disturbance torque during attitude maneuvers, as formulated in Section 2.3. To compensate for this effect, this section presents a quaternion-based attitude control framework that combines a baseline proportional-derivative (PD) control law with a feedforward gravity-torque compensation term. The compensation term is constructed using the final FRAMBO estimate, $\hat{\mathbf{r}}_{cg}$. The resulting commanded control torque is then converted into reaction wheel commands for the three orthogonally mounted reaction wheel assemblies.

4.1. Quaternion-Based Attitude Error Definition

The attitude error is defined using unit quaternions following the conventional quaternion feedback formulation [19,20]. In this study, a quaternion is represented using the scalar-last convention as

$$\mathbf{q} = \begin{bmatrix} \mathbf{q}_v^T & q_4 \end{bmatrix}^T = \begin{bmatrix} q_1 & q_2 & q_3 & q_4 \end{bmatrix}^T, \tag{32}$$

where $\mathbf{q}_v = [q_1\ q_2\ q_3]^T$ is the vector part and q_4 is the scalar part. Let the current attitude quaternion and the target attitude quaternion be denoted by $\mathbf{q}_s$ and $\mathbf{q}_t$, respectively:

$$\mathbf{q}_s = \begin{bmatrix} \mathbf{q}_{s,v}^T & q_{s,4} \end{bmatrix}^T, \qquad \mathbf{q}_t = \begin{bmatrix} \mathbf{q}_{t,v}^T & q_{t,4} \end{bmatrix}^T. \tag{33}$$

The attitude error quaternion is computed as

$$\mathbf{q}_e = (\mathbf{q}_t^{-1})^{\otimes} \mathbf{q}_s, \tag{34}$$

where $(\cdot)^{\otimes}$ denotes the quaternion multiplication matrix operator. The error quaternion is written as

$$\mathbf{q}_e = \begin{bmatrix} \mathbf{q}_{e,v}^T & q_{e,4} \end{bmatrix}^T. \tag{35}$$

To avoid the ambiguity caused by the double covering property of quaternions, the error quaternion is selected such that $q_{e,4} \geq 0$. If $q_{e,4} < 0$, the sign of $\mathbf{q}_e$ is reversed. The vector part $\mathbf{q}_{e,v}$ is then used as the attitude error input for the quaternion proportional-derivative controller developed in the following subsection.

4.2. Baseline Quaternion PD Controller

Using the attitude error definition in Section 4.1, the baseline attitude controller is formulated as a quaternion proportional-derivative (PD) controller. The angular velocity error is defined as

$$\boldsymbol{\omega}_e = \boldsymbol{\omega}_c - \boldsymbol{\omega}, \tag{36}$$

where $\boldsymbol{\omega}_c$ is the commanded angular velocity and $\boldsymbol{\omega}$ is the measured angular velocity, both expressed in $\mathcal{F}_B$. The commanded control torque is given by

$$\boldsymbol{\tau}_{PD} = -\mathbf{K}_p \mathbf{q}_{e,v} - \mathbf{K}_d \boldsymbol{\omega}_e, \tag{37}$$

where $\mathbf{q}_{e,v}$ is the vector part of the attitude error quaternion, $\boldsymbol{\omega}_e$ is the angular velocity error, and $\mathbf{K}_p$ and $\mathbf{K}_d$ are the proportional and derivative gain matrices, respectively. In this study, the target attitude is fixed during the commanded maneuver, and the desired angular velocity is set to zero.

The baseline controller provides the nominal attitude control torque without explicitly considering the residual gravity disturbance torque caused by the CR-CG offset. Therefore, in the presence of a nonzero $\mathbf{r}_{cg}$, the closed-loop response can be affected by the persistent gravity-induced disturbance. This limitation motivates the feedforward gravity-torque compensation term introduced in the following subsection.

4.3. Feedforward Gravity Torque Compensation Using Estimated CR-CG Offset

The baseline quaternion PD controller does not explicitly account for the residual gravity disturbance torque generated by the remaining CR-CG offset. After the FRAMBO stage, the final estimated offset vector, $\hat{\mathbf{r}}_{cg}$, is therefore used to construct a feedforward compensation term. Using the gravity torque model in Section 2.3, the estimated gravity disturbance torque is given by

$$\hat{\boldsymbol{\tau}}_g = \hat{\mathbf{r}}_{cg}{}^{\times}(m_{\text{tot}}\mathbf{g}_B). \tag{38}$$

To compensate for this disturbance, the commanded control torque applied to the platform is defined as

$$\boldsymbol{\tau}_c = \boldsymbol{\tau}_{PD} - \hat{\boldsymbol{\tau}}_g. \tag{39}$$

Substituting the baseline PD control law yields

$$\boldsymbol{\tau}_c = -\mathbf{K}_p\mathbf{q}_{e,v} - \mathbf{K}_d\boldsymbol{\omega}_e - \hat{\mathbf{r}}_{cg}{}^{\times}(m_{\text{tot}}\mathbf{g}_B). \tag{40}$$

Here, $\hat{\mathbf{r}}_{cg}$ is treated as a constant offset estimate during the attitude control experiment, whereas $\mathbf{g}_B$ varies with the platform attitude. Therefore, the compensation torque is updated according to the measured attitude through the transformation of the gravity vector into the body-fixed frame. This feedforward term reduces the effect of the residual gravity disturbance torque while preserving the feedback stabilization provided by the quaternion PD controller.

4.4. Reaction Wheel Torque Command Generation

Figure 10 shows the three-axis orthogonal reaction wheel configuration used in the attitude control experiment. The compensated platform control torque, $\boldsymbol{\tau}_c$, is generated by three reaction wheel assemblies mounted along the body-fixed x, y, and z axes. Since one reaction wheel is assigned to each body-fixed axis, no redundant control allocation is required, and the commanded platform torque can be directly mapped to the wheel axes.

Let the torque applied to the reaction wheel rotors be denoted by

$$\boldsymbol{\tau}_{rw} = \begin{bmatrix} \tau_{rw,x} & \tau_{rw,y} & \tau_{rw,z} \end{bmatrix}^T. \tag{41}$$

Because the torque applied to each wheel rotor produces an equal and opposite reaction torque on the platform, the relationship between the platform control torque and the wheel torque is given by

$$\boldsymbol{\tau}_c = -\boldsymbol{\tau}_{rw}. \tag{42}$$

Therefore, the wheel torque command is computed as

$$\boldsymbol{\tau}_{rw,cmd} = -\boldsymbol{\tau}_c. \tag{43}$$

For the i-th reaction wheel, the torque generated by wheel acceleration is modeled as

$$\tau_{rw,i} = J_{rw}\dot{\Omega}_i, \qquad i \in \{x, y, z\}, \tag{44}$$

where J_{rw} is the wheel inertia and Ω_i is the wheel angular speed. With a discrete control period Δt, the corresponding wheel-speed increment is obtained as

$$\Delta\Omega_{i,cmd} = \frac{\tau_{rw,i,cmd}}{J_{rw}}\Delta t. \tag{45}$$

The wheel-speed command is then updated as

$$\Omega_{i,cmd}(k+1) = \Omega_{i,cmd}(k) + \Delta\Omega_{i,cmd}. \tag{46}$$

In the implementation, the wheel-speed command is limited by the maximum allowable wheel speed and torque capability of the reaction wheel assembly. These saturation limits prevent excessive wheel acceleration and ensure that the generated control torque remains within the operational range summarized in Table 1.

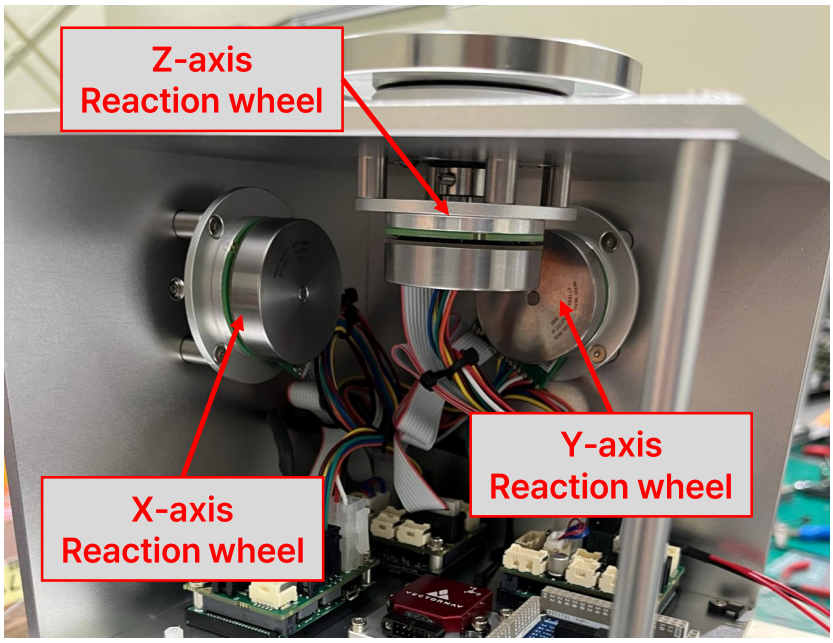

Figure 10. Three-axis orthogonal reaction wheel configuration used for attitude control torque generation.

5. Validation Results

This section validates the proposed two-stage mass balancing and gravity-compensated attitude control framework through numerical simulation and hardware experiments. First, the validation setup is described. The CRAMBO and FRAMBO results are then presented to evaluate the convergence of the estimated CR-CG offset. Finally, the attitude control performance is assessed through a comparison with the baseline controller and a coupled three-axis diagonal maneuver experiment on the 3-DoF spacecraft attitude simulator.

5.1. Experimental and Simulation Setup

The proposed RAMBO-based mass balancing and gravity-compensated attitude control framework was validated through hardware experiments and numerical simulation. The validation consisted of three parts: RAMBO-based mass balancing, simulation-based comparison of the baseline and proposed attitude controllers, and hardware attitude-control testing using the final balanced configuration. First, the CRAMBO and FRAMBO procedures were applied to reduce the residual CR-CG offset of the floating platform. The admissible CR-CG offset conditions and decision-logic parameters used in RAMBO are summarized in Table 4. These parameters define the balancing requirements, target vertical offsets, estimation windows, and weighting factors used in the mass balancing experiment. After the mass balancing procedure was completed, the final FRAMBO estimate of the CR-CG offset was

used as the residual imbalance condition for attitude-control validation. In the numerical simulation, the rigid-body rotational dynamics described in Section 2.4 were used, and the gravity disturbance torque was generated using the model in Section 2.3. The simulation compared the baseline quaternion PD controller without gravity-torque compensation and the proposed controller with feedforward gravity-torque compensation. To reflect the sensing conditions of the hardware implementation, attitude and angular-rate measurement noise corresponding to the IMU characteristics was included in the simulation. The same attitude-control conditions were then used in the hardware experiment. The controller was implemented using three orthogonally mounted reaction wheel assemblies, and the maneuver command was defined as a coupled three-axis diagonal attitude command from $(0^\circ, 0^\circ, 0^\circ)$ to $(15^\circ, -10^\circ, 35^\circ)$. The attitude-control requirements, controller gains, test case, and control deadbands are summarized in Table 5. The main performance metrics were the estimated CR-CG offset, attitude response, tracking error, angular velocity error, and reaction wheel speed response.

Table 4. RAMBO admissible conditions and decision-logic parameters.

Category	Parameter	Value	Unit
Requirement	CRAMBO lateral admissible condition	$\lvert\hat{x}_{cg}\rvert,\ \lvert\hat{y}_{cg}\rvert < 1$	µm
	CRAMBO vertical admissible range	$-100 < \hat{z}_{cg} < -70$	µm
	FRAMBO lateral admissible condition	$\lvert\hat{x}_{cg}\rvert,\ \lvert\hat{y}_{cg}\rvert < 0.5$	µm
	FRAMBO vertical admissible range	$-30 < \hat{z}_{cg} < -20$	µm
Control	IMU sampling rate	50	Hz
CRAMBO	Target vertical offset, $\hat{z}_{cg,tar}$	-75	µm
	Estimation window, $t_{C,\mathrm{win}}$	40	sec
	Intermediate vertical bounds, $\beta_{C,k}$	$-100,\ -70,\ -100$	µm
	Lateral weighting factor, $w_{C,\alpha}$	0.5	–
	Vertical weighting factors, $w_{C,\beta,k}$	0.6, 0.6	–
FRAMBO	Target vertical offset, $\hat{z}_{cg,tar}$	-25	µm
	Estimation window, $t_{F,\mathrm{win}}$	80	sec
	Intermediate vertical bounds, $\beta_{F,k}$	$-100,\ -20,\ -100,\ -50,\ -20$	µm
	Lateral weighting factor, $w_{F,\alpha}$	0.5	–
	Vertical weighting factors, $w_{F,\beta,k}$	0.3, 0.6, 0.3, 0.3	–

Table 5. Attitude-control test conditions and controller parameters.

Category	Parameter	Value	Unit
Requirement	Attitude error	< 1	deg
	Angular velocity error	< 0.5	deg/s
Control	IMU sampling rate	50	Hz
	RW command/encoder communication rate	5	Hz
	RW speed command update interval	1.0	s
	Proportional gain, $\mathbf{K}_p$	$\mathrm{diag}([0.27,\ 0.28,\ 0.10])$	N·m
	Derivative gain, $\mathbf{K}_d$	$\mathrm{diag}([1.00,\ 1.04,\ 0.36])$	N·m·s
Test case	Initial attitude	$[0,\ 0,\ 0]^T$	deg
	Target attitude	$[15,\ -10,\ 35]^T$	deg
	Target angular velocity	$[0,\ 0,\ 0]^T$	deg/s
Control deadband	Attitude error deadband	0.3	deg
	Angular velocity error deadband	0.3	deg/s

Although the RW command/encoder communication was performed at 5 Hz, the wheel-speed command value was updated every 1.0 s and held constant between updates. This command update interval was selected to allow the reaction wheel speed response to settle sufficiently before the next command update, as illustrated in Fig. 11.

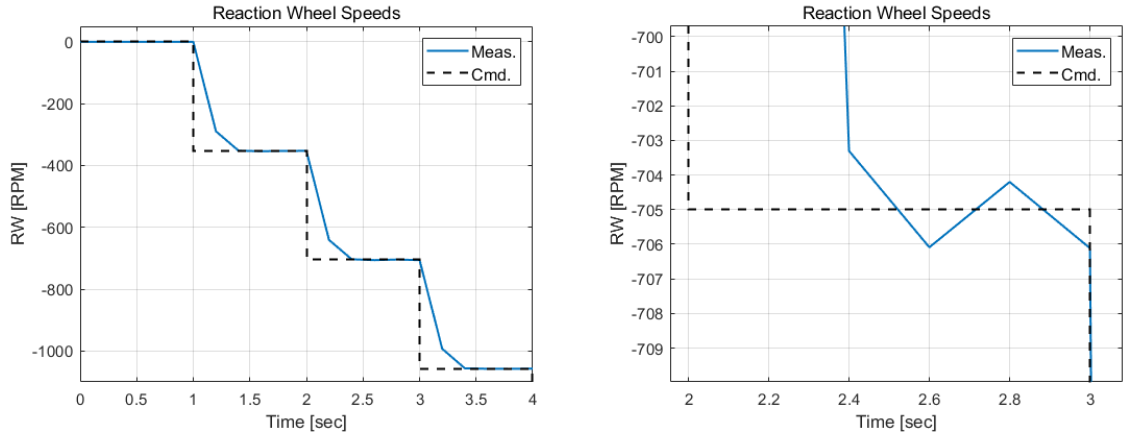

(**a**) (**b**)

Figure 11. Reaction wheel speed response used to justify the wheel-speed command update interval: (**a**) overall command and measured speed response; (**b**) enlarged view showing speed settling within one command update interval.

5.2. CRAMBO/FRAMBO Mass Balancing Results

The mass balancing performance of the proposed RAMBO procedure was evaluated by sequentially applying the CRAMBO and FRAMBO stages. Before CRAMBO, the platform was manually pre-balanced to avoid excessive initial tipping motion. Therefore, the results presented in this subsection should be interpreted as automatic reduction and refinement of the remaining residual CR-CG offset rather than recovery from a severely unbalanced condition. Table 6 summarizes the estimated CR-CG offset before and after each RAMBO stage. CRAMBO reduced the vertical offset from approximately -265.142 µm to -95.083 µm, while maintaining the lateral components at the micrometer level. FRAMBO further refined the residual offset, resulting in a final estimate of approximately $[0.083,\ 0.115,\ -27.621]^T$ µm. These results show that RAMBO reduced the estimated lateral CR-CG offset to a sub-micrometer level while maintaining a negative vertical offset for pendulum-like stability. Detailed iteration- and trial-level balancing records are provided in Appendix A.

Table 6. Summary of CR-CG offset convergence before and after each RAMBO stage.

Stage	Executions	Initial $\hat{\mathbf{r}}_{cg}$ [µm]	Final $\hat{\mathbf{r}}_{cg}$ [µm]
CRAMBO	8 iterations	$[1.562,\ 1.810,\ -265.142]^T$	$[0.303,\ 0.005,\ -95.083]^T$
FRAMBO	11 trials	$[0.232,\ 0.393,\ -84.363]^T$	$[0.083,\ 0.115,\ -27.621]^T$

As a consistency check for the final balanced condition, the last two FRAMBO trials were examined using the detailed records in Table A2. In Trials 10 and 11, no additional slider command was applied, and the corresponding estimates were $[0.0848,\ 0.0938,\ -23.1258]^T$ µm and $[0.0830,\ 0.1146,\ -27.6205]^T$ µm, respectively. Both estimates remained within the prescribed fine admissible range, indicating that the final balanced condition was consistently identified by the proposed free-response estimation procedure. Figure 12 shows the estimated CR-CG offset convergence during the CRAMBO balancing test. The lateral components remained within a few micrometers, while the vertical component was rapidly shifted toward a less negative but still stable range. This

behavior reflects the role of CRAMBO as a coarse balancing stage that reduces the initial residual imbalance without attempting final fine tuning.

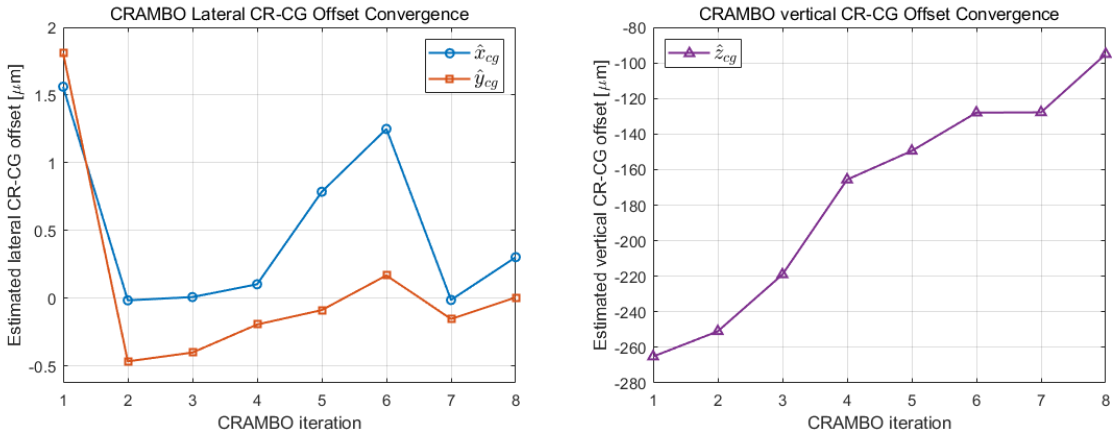

(**a**) (**b**)

Figure 12. Estimated CR-CG offset convergence during the CRAMBO balancing test: (**a**) lateral components; (**b**) vertical component.

Figure 13 shows the estimated CR-CG offset convergence during the FRAMBO balancing test. Compared with CRAMBO, FRAMBO used smaller correction commands and platform reinitialization between trials. Although trial-to-trial variations were observed because of estimation uncertainty and axis-to-axis coupling, the final lateral offset components converged to the sub-micrometer level, and the vertical offset settled near the desired negative range.

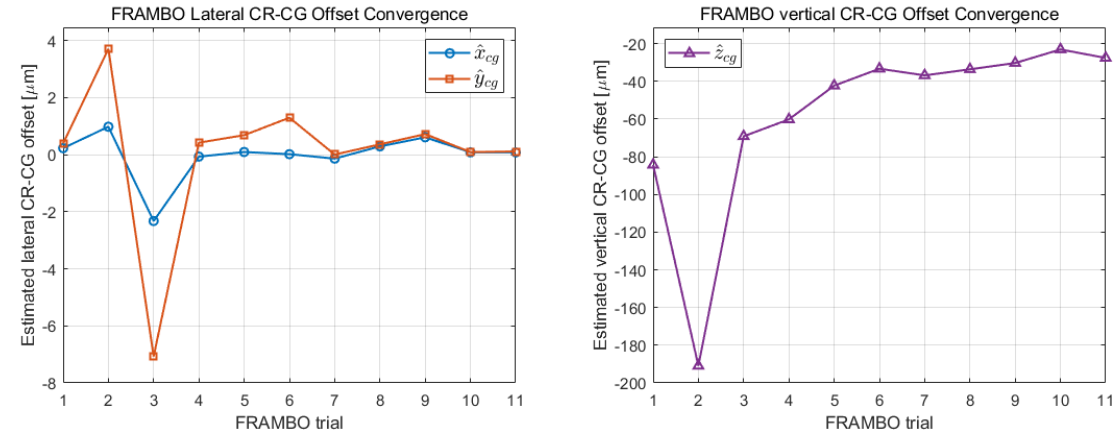

(**a**) (**b**)

Figure 13. Estimated CR-CG offset convergence during the FRAMBO balancing test: (**a**) lateral components; (**b**) vertical component.

To examine the resulting passive platform behavior, free-response roll and pitch responses were compared before CRAMBO and after FRAMBO, as shown in Figure 14. The post-FRAMBO response does not necessarily exhibit a smaller angular amplitude because the vertical offset was moved closer to zero. For a hemispherical air-bearing platform, reducing $|z_{cg}|$ decreases the passive pendulum stiffness, which can increase the angular sensitivity to the remaining lateral offset. Therefore, the free-response result should be interpreted together with the estimated CR-CG offset convergence.

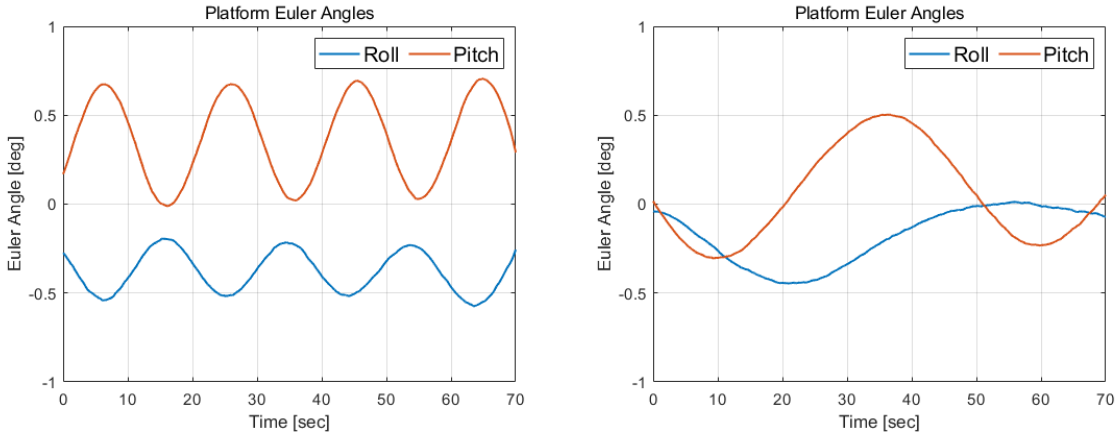

(**a**) (**b**)

Figure 14. Free-response roll and pitch responses before and after automatic mass balancing: (**a**) manually pre-balanced condition before CRAMBO; (**b**) final balanced condition after FRAMBO.

For a quantitative comparison, the roll–pitch oscillation was evaluated using peak amplitudes and the dominant period. The peak amplitudes were computed after subtracting the mean value of each free-response signal. Starting from the Euler rotational equation with the gravity torque, the small-angle roll–pitch motion of the platform can be approximated by an equivalent pendulum model as

$$J_{\mathrm{eq}}\ddot{\theta} + k_\theta \theta = 0, \qquad k_\theta \approx m_{\mathrm{tot}} g h, \qquad T = \frac{2\pi}{\sqrt{k_\theta / J_{\mathrm{eq}}}}, \tag{47}$$

where $h = |z_{cg}|$, J_{eq} is the equivalent roll–pitch inertia, and T is the dominant oscillation period. Based on this approximation, the relative stiffness and equivalent pendulum-mode energy ratios can be estimated as

$$\frac{k_{\theta,a}}{k_{\theta,b}} \approx \left(\frac{T_b}{T_a}\right)^2, \qquad \frac{E_a}{E_b} \approx \left(\frac{\theta_{rp,a}}{\theta_{rp,b}}\right)^2 \left(\frac{T_b}{T_a}\right)^2, \tag{48}$$

where the subscripts b and a denote the conditions before CRAMBO and after FRAMBO, respectively, and θ_{rp} is the combined roll–pitch peak amplitude.

Table 7 summarizes the free-response comparison. Although the combined peak amplitude increased from 0.3801° to 0.4985°, the dominant period increased from 20 s to 50 s. As a result, the estimated equivalent pendulum-mode energy after FRAMBO was approximately 27.5% of the pre-CRAMBO value, corresponding to a 72.5% reduction. This indicates that the final balancing condition reduced the effective pendulum-mode energy while maintaining a bounded and stable free-response behavior.

Table 7. Free-response roll–pitch oscillation comparison before CRAMBO and after FRAMBO.

Condition	Roll peak [deg]	Pitch peak [deg]	Combined peak [deg]	Dominant period [s]	Stiffness ratio	Energy ratio
Before CRAMBO	0.1901	0.3291	0.3801	20	1.000	1.000
After FRAMBO	0.1894	0.4612	0.4985	50	0.160	0.275

5.3. Simulation Comparison: Baseline PD vs Proposed Controller

A numerical simulation was conducted to evaluate the effect of the feedforward gravity-torque compensation term independently from hardware implementation effects. The final CR-CG offset estimate obtained in Section 5.2, $\hat{\mathbf{r}}_{cg} = [0.083,\ 0.115,\ -27.621]^T$ µm, was used as the residual imbalance condition in the simulation. The baseline controller was defined as the quaternion PD controller without gravity-torque compensation, whereas the proposed controller included the feedforward

compensation term constructed from $\hat{\mathbf{r}}_{cg}$. Both controllers were tested under the same maneuver command from $(0°, 0°, 0°)$ to $(15°, -10°, 35°)$. To reflect the sensing conditions of the hardware implementation, attitude and angular-rate measurement noise corresponding to the IMU characteristics was included in the simulation. Figure 15 compares the Euler angle responses and tracking errors of the baseline PD controller and the proposed gravity-compensated PD controller. The effect of the feedforward compensation was most pronounced in the roll and pitch axes, where the residual gravity disturbance torque directly affects the pendulum-like motion of the platform. In the roll axis, the steady-state tracking error was reduced from approximately $-0.8°$ for the baseline PD controller to approximately $0.1°$ with the proposed controller. In the pitch axis, the steady-state error was reduced from approximately $0.5°$ to approximately $0.05°$. In contrast, the yaw response showed only a marginal difference between the two controllers because the yaw-axis motion is less directly affected by the gravity vector. These results indicate that the feedforward gravity-torque compensation term effectively reduces the residual roll and pitch attitude errors caused by the remaining CR-CG offset.

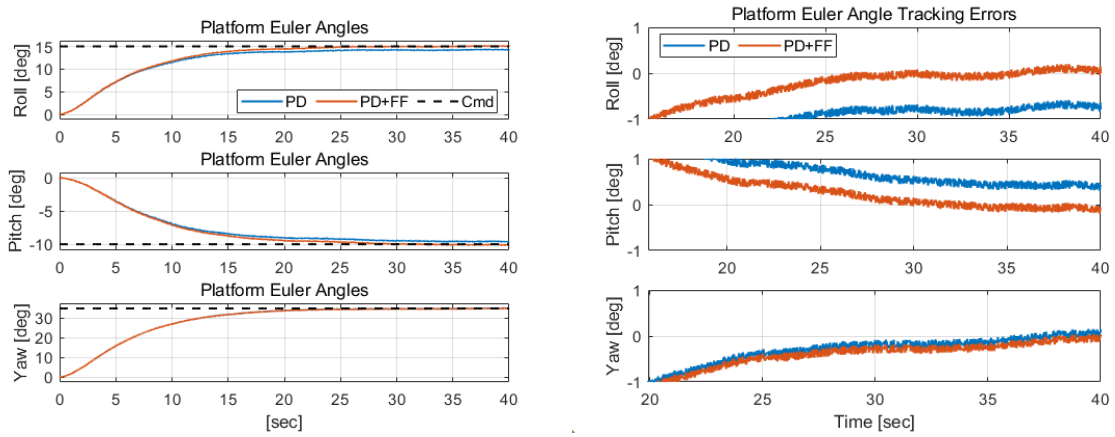

Figure 15. Simulation comparison of Euler angle responses and tracking errors with and without feedforward gravity-torque compensation: (**a**) Euler angle response; (**b**) Euler angle tracking error.

5.4. Three-Axis Diagonal Maneuver Experiment and Tracking Error Analysis

After the CRAMBO and FRAMBO stages, a three-axis diagonal attitude maneuver was conducted on the hardware testbed to validate the proposed gravity-compensated attitude controller. The initial attitude command was set to $(0°, 0°, 0°)$, and the target attitude command was set to $(15°, -10°, 35°)$ in roll, pitch, and yaw, respectively. During the experiment, the final CR-CG offset estimate obtained from FRAMBO was used in the feedforward gravity-torque compensation term. Figure 16 shows the platform attitude response and the corresponding attitude tracking error during the diagonal maneuver. The roll, pitch, and yaw angles followed the commanded attitude trajectory and converged toward the target attitude without loss of stability. After the transient response, the attitude tracking errors computed from the primary onboard VN-100 estimates remained within approximately $\pm 0.5°$, indicating that the proposed gravity-compensated controller achieved a sub-degree-level steady-state response under the residual gravity disturbance condition.

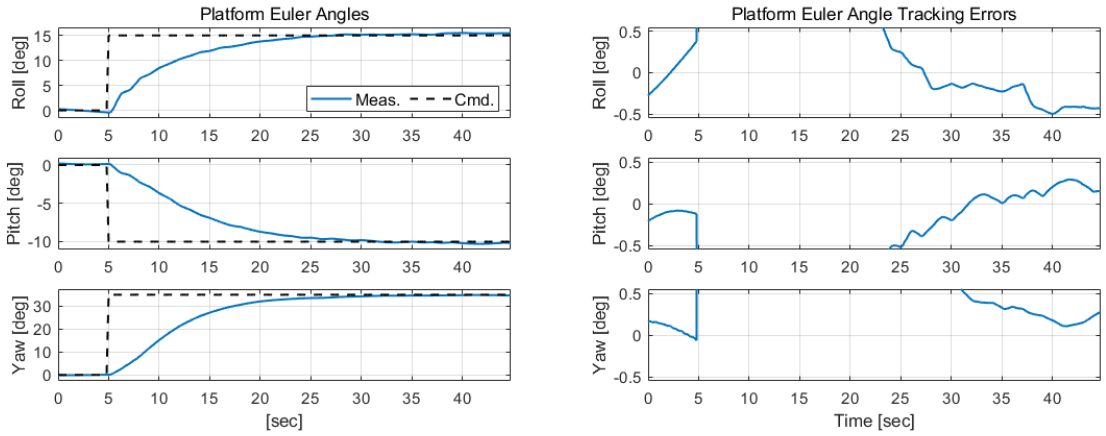

(**a**) (**b**)

Figure 16. Platform attitude response and attitude tracking error during the three-axis diagonal maneuver: (**a**) Euler angle response; (**b**) Euler angle tracking error.

To provide an additional roll/pitch consistency check, the attitude response was compared with measurements from a secondary WITMotion IMU, as shown in Fig. 17. The secondary IMU data were used only for roll/pitch relative-motion comparison after initial offset removal and sign-convention correction. The yaw output was excluded because the heading estimate of the secondary IMU was unreliable in the experimental magnetic environment. This comparison is used as a secondary consistency check rather than as an independent ground-truth validation.

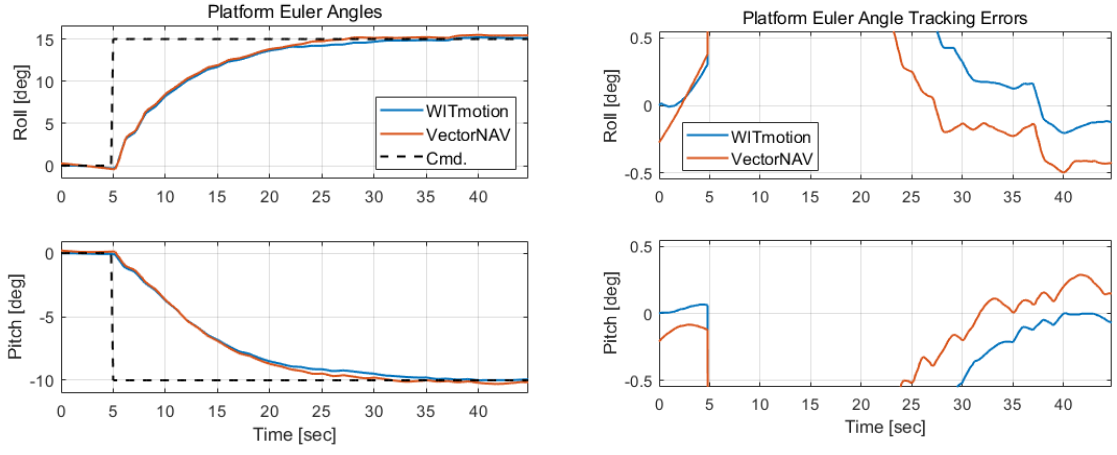

(**a**) (**b**)

Figure 17. Roll/pitch consistency check using the secondary WITMotion IMU: (**a**) roll/pitch response comparison with the VN-100 and command; (**b**) roll/pitch tracking error comparison between the VN-100 and WITMotion.

Figure 18 presents the platform angular velocity response and the corresponding angular velocity tracking error. The angular velocities increased during the transient maneuver phase and decreased as the attitude approached the target command. Based on the VN-100 angular-rate estimates, the residual angular velocity error after convergence was maintained within approximately $\pm 0.4^\circ/\mathrm{s}$ for the roll axis and within approximately $\pm 0.2^\circ/\mathrm{s}$ for the pitch and yaw axes. Although small residual oscillations remained because of hardware limitations and unmodeled disturbances, the angular velocity errors were bounded throughout the steady-state response.

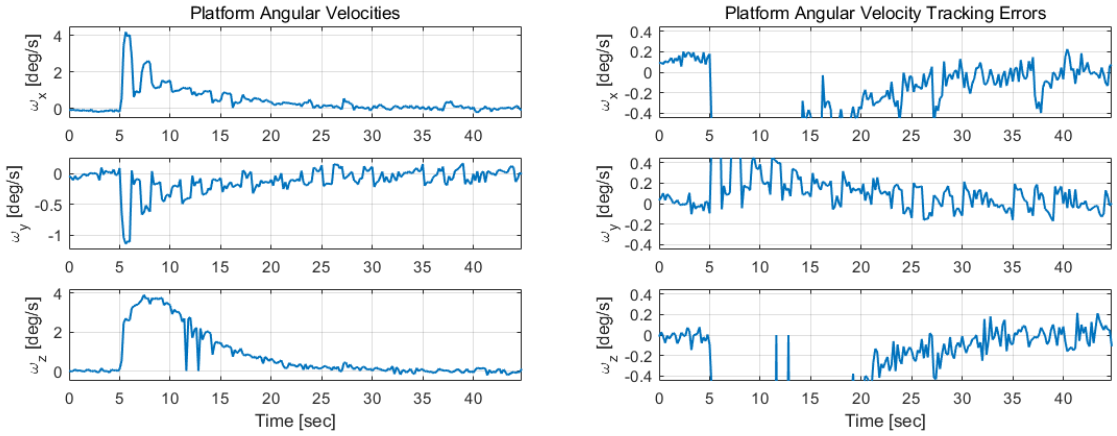

(**a**) (**b**)

Figure 18. Platform angular velocity response and angular velocity tracking error during the three-axis diagonal maneuver: (**a**) angular velocity response; (**b**) angular velocity tracking error.

Figure 19 shows the commanded and measured reaction wheel speeds during the maneuver. The wheel speeds remained within the allowable operating range while generating the required control torque for the coupled three-axis attitude maneuver. This confirms that the proposed control command was feasible for the three orthogonally mounted reaction wheel assemblies.

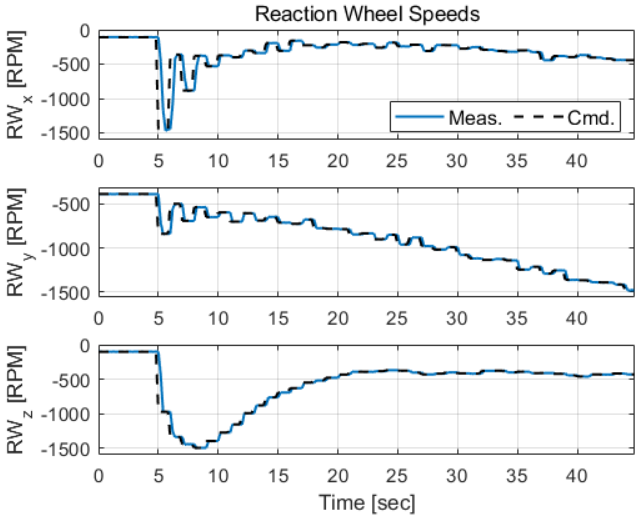

Figure 19. Reaction wheel speed commands and measured wheel speeds during the three-axis diagonal maneuver.

Overall, the experimental results demonstrate that the proposed two-stage mass balancing and feedforward gravity-torque compensation approach enables stable three-axis attitude control on the 3-DoF air-bearing simulator. The final attitude and angular velocity errors satisfy the intended experimental performance range based on the onboard VN-100 estimates, while the secondary IMU roll/pitch comparison provides an additional consistency check. These results indicate that sub-degree-level onboard-IMU-estimated stabilization can be achieved even when a small estimated residual CR-CG offset remains after mass balancing.

6. Discussion

6.1. Residual CR-CG Offset and Stability Trade-off

The experimental results show that the proposed RAMBO procedure reduces the CR-CG offset to a level that enables stable three-axis attitude control experiments. However, the objective of the balancing

process is not to force the CR-CG offset vector, $\mathbf{r}_{cg}$, to become exactly zero. In the hemispherical air-bearing platform, a small negative vertical offset is intentionally maintained to provide a pendulum-like restoring tendency and to reduce the risk of tipping instability. Therefore, the final balancing condition represents a trade-off between minimizing the residual gravity disturbance torque and maintaining passive platform stability. As discussed in Section 2.3, the residual gravity disturbance torque depends on both the CR-CG offset and the gravity vector expressed in the body-fixed frame. The bounded attitude and angular velocity responses observed in the hardware experiment indicate that the final FRAMBO estimate, $\hat{\mathbf{r}}_{cg}$, provides a sufficiently stable and compensable residual imbalance condition. This supports the use of $\hat{\mathbf{r}}_{cg}$ not only as a balancing performance indicator but also as a feedforward compensation parameter for attitude control.

6.2. Hardware Non-Idealities and Implementation Limits

The performance of RAMBO is affected by practical hardware non-idealities. In the mass balancing mechanism, small geometric misalignments, assembly tolerances, and slider installation errors can make the physical sliding axes non-orthogonal with respect to the body-fixed frame. As a result, a command applied to one sliding mass may affect multiple components of the CR-CG offset. This axis-to-axis coupling motivates the two-stage structure of CRAMBO and FRAMBO, where coarse automatic correction is followed by fine correction with platform reinitialization. In this study, the full non-orthogonal slider-axis matrix, $\mathbf{U}_s$, was not separately identified. Therefore, RAMBO should not be interpreted as a geometric calibration method that explicitly inverts the non-orthogonal slider kinematics. Instead, the slider command is generated from a nominal diagonal mass-shift relation, and the remaining coupling effects are reduced operationally through repeated least-squares estimation, conservative weighting, and stop-and-restart fine balancing. Similar non-idealities also exist in the reaction wheel assemblies. Although the controller assumes that the reaction wheel axes are aligned with the body-fixed axes, small mounting errors, wheel-disk imbalance, and actuator imperfections may remain in the real hardware. These effects were not separately identified in this study and may contribute to the residual attitude and angular velocity oscillations observed after convergence. In addition, although RW command/encoder communication was performed at 5 Hz, the wheel-speed command value was updated at 1.0 s intervals in the present implementation to allow the wheel-speed response to settle between command updates. This conservative command scheduling was sufficient for the present diagonal maneuver experiment, but higher-bandwidth attitude-control tests would require faster command updating together with explicit consideration of the reaction wheel speed-response dynamics.

6.3. Sensing Dependency and Applicability to Ground-Based ADCS Validation

The proposed framework relies on IMU-based attitude and angular velocity measurements for both CR-CG offset estimation and attitude control. Therefore, IMU noise, bias drift, and attitude estimation errors can affect the least-squares-based balancing result as well as the closed-loop control performance. The RAMBO procedure in this study should therefore be interpreted as a pre-test/intermittent balancing procedure rather than as a continuous online mass redistribution scheme during attitude control. The final FRAMBO estimate is treated as a constant parameter during the subsequent maneuver, and possible time-varying changes in mass distribution, thermal drift, or mechanical drift are not estimated online. The validation was performed within the allowable angular motion range of the hemispherical air-bearing platform. Therefore, the results should be interpreted as ground-based ADCS validation results rather than direct in-orbit performance. Future improvements may include calibration of the non-orthogonal sliding axes, identification of reaction wheel alignment and imbalance effects, incorporation of additional attitude reference sensors, higher-rate reaction wheel command updates, and online update of the CR-CG offset during attitude control operation.

7. Conclusions

This paper presented a two-stage automatic mass balancing and gravity-compensated attitude control framework for a hemispherical air-bearing-based three-degree-of-freedom spacecraft attitude simulator. The proposed Robust Automatic Mass Balancing Operator (RAMBO) consists of a coarse balancing stage, CRAMBO, and a fine balancing stage, FRAMBO. CRAMBO rapidly reduces the initial CR-CG offset through an automatic iterative loop, whereas FRAMBO refines the remaining offset using batch least-squares-based estimation and stop-and-restart operation. The framework was designed to address practical hardware constraints, including residual CR-CG offset, non-ideal mass balancing mechanisms, and the need to maintain a negative vertical offset for passive pendulum-like stability. The validation results showed that the CRAMBO stage was completed after eight iterations, and the FRAMBO stage was completed after eleven trials. After the final FRAMBO stage, the estimated dynamic-equivalent CR-CG offset converged to approximately $[0.08,\ 0.12,\ -27.62]$ μm, indicating that the estimated lateral offset components were reduced to the micrometer level while the vertical offset remained in the desired negative range. The final FRAMBO estimate was then used to construct the feedforward gravity-torque compensation term in the quaternion PD controller. In the three-axis diagonal maneuver experiment from $(0^\circ, 0^\circ, 0^\circ)$ to $(15^\circ, -10^\circ, 35^\circ)$, the proposed controller achieved steady-state attitude errors within approximately $\pm 0.5^\circ$ based on the onboard VN-100 estimates, with the roll/pitch response additionally checked using a secondary IMU. The angular velocity errors based on the VN-100 angular-rate estimates remained within approximately $\pm 0.4^\circ/\mathrm{s}$ for roll and $\pm 0.2^\circ/\mathrm{s}$ for pitch and yaw. These results demonstrate that the proposed framework enables stable onboard-IMU-estimated three-axis attitude control experiments even when a small estimated residual gravity disturbance torque remains after mass balancing. Future work will focus on improving the fidelity and repeatability of the ground-based validation system. Vision-based attitude measurement will be introduced as an external ground-truth reference to reduce the dependency on IMU-only attitude determination and to enable more stringent mass balancing and attitude-control validation. In addition, CubeSat-class reaction wheel modules with lower angular momentum capacity will be integrated into the simulator to evaluate the proposed balancing and control framework under tighter actuator constraints. Under such limited-momentum conditions, more accurate CR-CG offset reduction and disturbance compensation will be required for stable attitude-control operation.

Funding: This research received no external funding.

Data Availability Statement: The data presented in this study are available from the corresponding author upon reasonable request.

Conflicts of Interest: The authors declare no conflicts of interest.

Appendix A. Detailed RAMBO Balancing Results

Tables A1 and A2 summarize the detailed CRAMBO and FRAMBO balancing records. Here, $\Delta s_{\mathrm{raw},i}$ denotes the correction value computed before decision weighting, $\Delta s_{\mathrm{cmd},i}$ denotes the applied slider command after the RAMBO decision logic, and enc_i denotes the accumulated encoder position.

Table A1. Detailed CRAMBO balancing records. The estimated CR-CG offsets are given in μm, and the slider commands and encoder positions are given in degrees.

Iter.	$\hat{x}_{cg}$ [μm]	$\hat{y}_{cg}$ [μm]	$\hat{z}_{cg}$ [μm]	$\Delta s_{\mathrm{raw},x}$ [deg]	$\Delta s_{\mathrm{raw},y}$ [deg]	$\Delta s_{\mathrm{raw},z}$ [deg]	$\Delta s_{\mathrm{cmd},x}$ [deg]	$\Delta s_{\mathrm{cmd},y}$ [deg]	$\Delta s_{\mathrm{cmd},z}$ [deg]	enc_x [deg]	enc_y [deg]	enc_z [deg]
1	1.5615	1.8100	-265.142	-10.2207	-11.8470	1806.0982	10.2207	11.8470	0	10.044	11.628	0
2	-0.0156	-0.4661	-250.971	0.1020	3.0507	1671.4923	0	0	-360	10.044	11.628	-359.856
3	0.0088	-0.4010	-219.011	-0.0574	2.6250	1367.9145	0	0	-360	10.044	11.628	-719.856
4	0.1030	-0.1940	-165.652	-0.6745	1.2699	861.0744	0	0	-360	10.044	11.628	-1079.86
5	0.7859	-0.0877	-149.482	-5.1442	0.5739	707.4807	0	0	-360	10.044	11.628	-1439.82
6	1.2497	0.1684	-127.977	-8.1797	-1.1021	503.2116	8.1797	1.1021	0	18.180	12.744	-1439.86
7	-0.0128	-0.1532	-127.820	0.0839	1.0029	501.7203	0	0	-360	18.180	12.744	-1799.86
8	0.3035	0.0054	-95.0828	-1.9865	-0.0353	190.7601	0	0	0	18.180	12.744	-1799.86

Table A2. Detailed FRAMBO balancing records. The estimated CR-CG offsets are given in μm, and the slider commands and encoder positions are given in degrees.

Trial	$\hat{x}_{cg}$ [μm]	$\hat{y}_{cg}$ [μm]	$\hat{z}_{cg}$ [μm]	$\Delta s_{\text{raw},x}$ [deg]	$\Delta s_{\text{raw},y}$ [deg]	$\Delta s_{\text{raw},z}$ [deg]	$\Delta s_{\text{cmd},x}$ [deg]	$\Delta s_{\text{cmd},y}$ [deg]	$\Delta s_{\text{cmd},z}$ [deg]	enc_x [deg]	enc_y [deg]	enc_z [deg]
1	0.2316	0.3934	-84.3363	-1.5157	-2.5751	563.6170	0	0	-338.1700	0	0	-338.184
2	0.9817	3.7124	-190.9290	-6.4257	-24.2996	1576.1100	6.4257	24.2996	0	6.408	24.228	-338.184
3	-2.3233	-7.0698	-69.1763	15.2070	46.2752	419.6170	-7.6035	-23.1376	0	-0.972	1.404	-338.184
4	-0.0652	0.4231	-60.2105	0.4268	-2.7693	334.4540	0	0	-200.6724	-0.972	1.404	-538.814
5	0.0958	0.6867	-42.3175	-0.6271	-4.4945	164.4940	0	0	-49.3481	-0.972	1.404	-587.810
6	0.0207	1.2984	-33.3349	-0.1354	-8.4986	79.1702	0	4.2493	0	-0.972	5.328	-587.810
7	-0.1358	0.0075	-36.8673	0.8891	-0.0490	112.7240	0	0	-33.8171	-0.972	5.328	-621.542
8	0.2929	0.3646	-33.6496	-1.9175	-2.3862	82.1594	0	0	-24.6478	-0.972	5.328	-646.094
9	0.6119	0.7235	-30.3074	-4.0053	-4.7358	50.4133	2.0027	2.3679	0	1.116	7.678	-646.094
10	0.0848	0.0938	-23.1258	-0.5551	-0.6139	-17.8027	0	0	0	1.116	7.628	-646.094
11	0.0830	0.1146	-27.6205	-0.5432	-0.7502	24.8911	0	0	0	1.116	7.628	-646.094

References

1. Jung, D.; Tsiotras, P. A 3-DoF Experimental Test-Bed for Integrated Attitude Dynamics and Control Research. In Proceedings of the AIAA Guidance, Navigation, and Control Conference and Exhibit, Austin, Texas, 2003. AIAA Paper 2003-5331, https://doi.org/10.2514/6.2003-5331.
2. Thomas, D.; Wolosik, A.T.; Black, J. CubeSat Attitude Control Simulator Design. In Proceedings of the AIAA Modeling and Simulation Technologies Conference, Kissimmee, Florida, 2018. AIAA Paper 2018-1391, https://doi.org/10.2514/6.2018-1391.
3. da Silva, R.C.; Borges, R.A.; Battistini, S.; Cappelletti, C. A Review of Balancing Methods for Satellite Simulators. *Acta Astronautica* **2021**, *187*, 537–545. https://doi.org/10.1016/j.actaastro.2021.05.037.
4. Prado, J.; Bisiacchi, G.; Reyes, L.; Vicente, E.; Contreras, F.; Mesinas, M.; Juarez, A. Three-axis air-bearing based platform for small satellite attitude determination and control simulation. *Journal of Applied Research and Technology* **2005**, *3*, 222–237. https://doi.org/10.22201/icat.16656423.2005.3.03.563.
5. Peck, M.A.; Miller, L.; Cavender, A.R.; Gonzalez, M.; Hintz, T. An Airbearing-Based Testbed for Momentum-Control Systems and Spacecraft Line of Sight. In Proceedings of the 13th Annual AAS/AIAA Space Flight Mechanics Meeting, 2003, Vol. 114, *Advances in the Astronautical Sciences*, pp. 427–446. AAS Paper 03-127.
6. Jovanovic, N.; Pearce, J.M.; Praks, J. Design and Testing of a Low-Cost, Open Source, 3-D Printed Air-Bearing-Based Attitude Simulator for CubeSat Satellites. *Journal of Small Satellites* **2019**, *8*, 859–880. Available online: https://jossonline.com/wp-content/uploads/2021/08/Final-Jovanovic-Design-and-Testing-of-Low-Cost-Open-Source-3-D-Printed-Air-Bearing-Based-Attitude-Simulator-for-CubeSat-Satellites.pdf (accessed on 14 June 2026).
7. Inumoh, L.O.; Forshaw, J.L.; Horri, N.M. Tilted wheel satellite attitude control with air-bearing table experimental results. *Acta Astronautica* **2015**, *117*, 414–429. https://doi.org/10.1016/j.actaastro.2015.09.007.
8. Kim, J.J.; Agrawal, B.N. Automatic Mass Balancing of Air-Bearing-Based Three-Axis Rotational Spacecraft Simulator. *Journal of Guidance, Control, and Dynamics* **2009**, *32*, 1005–1017. https://doi.org/10.2514/1.34437.
9. Chesi, S.; Gong, Q.; Pellegrini, V.; Cristi, R.; Romano, M. Automatic Mass Balancing of a Spacecraft Three-Axis Simulator: Analysis and Experimentation. *Journal of Guidance, Control, and Dynamics* **2014**, *37*, 197–206. https://doi.org/10.2514/1.60380.
10. Contreras, J.P.; Arestegui, N.A.; Cayo, E.H.; Pumacota, E.M. Low Weight and Inertia Self-Balancing Testbed for a 3U CubeSat Attitude Control System. *IEEE Access* **2025**, *13*, 140392–140411. https://doi.org/10.1109/ACCESS.2025.3597232.
11. Boynton, R. Using a Spherical Air Bearing to Simulate Weightlessness. In Proceedings of the 55th Annual Conference of the Society of Allied Weight Engineers, 1996. SAWE Paper No. 2297. Available online: https://raptor-scientific.com/content/uploads/2020/10/Using_a_Spherical_Air_Bearing_to_Simulate_Weightlessness.pdf (accessed on 14 June 2026).
12. Li, Y.; Gao, Y. Equations of Motion for the Automatic Balancing System of 3-DOF Spacecraft Attitude Control Simulator. In Proceedings of the 2010 3rd International Symposium on Systems and Control in Aeronautics and Astronautics, Harbin, China, 2010; pp. 248–251. https://doi.org/10.1109/ISSCAA.2010.5633650.
13. Di Domenico, G.; Topputo, F. Disturbances Quantification for Air-Bearing Spacecraft Attitude Simulation Platforms. In Proceedings of the AIAA SCITECH 2024 Forum, 2024. AIAA Paper 2024-0379, https://doi.org/10.2514/6.2024-0379.
14. Bahu, A.; Modenini, D. Automatic mass balancing system for a dynamic CubeSat attitude simulator: development and experimental validation. *CEAS Space Journal* **2020**, *12*, 597–611. https://doi.org/10.1007/s12567-020-00309-5.

15. Xu, Z.; Qi, N.; Chen, Y. Parameter estimation of a three-axis spacecraft simulator using recursive least-squares approach with tracking differentiator and extended Kalman filter. *Acta Astronautica* **2015**, *117*, 254–262. https://doi.org/10.1016/j.actaastro.2015.08.010.
16. Krishnanunni, A.R.; Jayadevan, S.; Mony, A.; Sharma, G.N. Inertia and Center of Mass Estimation of a 3 DoF Air Bearing Platform. *IFAC-PapersOnLine* **2018**, *51*, 219–224. https://doi.org/10.1016/j.ifacol.2018.05.047.
17. Curatolo, A.; Bahu, A.; Modenini, D. Automatic Balancing for Satellite Simulators with Mixed Mechanical and Magnetic Actuation. *Aerospace* **2022**, *9*, 223. https://doi.org/10.3390/aerospace9040223.
18. Liu, Y.; Li, L.; Fu, Z.; Tan, J.; Li, K. Automatic Mass Balancing of a Spacecraft Simulator Based on Non-Orthogonal Structure. In Proceedings of the 2016 UKACC 11th International Conference on Control (CONTROL), Belfast, UK, 2016; pp. 1–6. https://doi.org/10.1109/CONTROL.2016.7737579.
19. Wie, B.; Weiss, H.; Arapostathis, A. Quaternion Feedback Regulator for Spacecraft Eigenaxis Rotations. *Journal of Guidance, Control, and Dynamics* **1989**, *12*, 375–380. https://doi.org/10.2514/3.20418.
20. Wie, B. *Space Vehicle Dynamics and Control*, 2nd ed.; American Institute of Aeronautics and Astronautics: Reston, Virginia, 2008. https://doi.org/10.2514/4.860119.
21. VectorNav Technologies. VN-100 IMU/AHRS, 2026. Online product specifications. Available online: https://www.vectornav.com/products/detail/vn-100 (accessed on 11 June 2026).
22. Physik Instrumente. A-65x Series Air Bearing Rotation Stages Datasheet, 2026. Available online: https://www.pikorea.co.kr/fileadmin/user_upload/physik_instrumente/files/datasheets/A-65x-Datasheet.pdf (accessed on 12 June 2026).
23. WITMotion. BWT901CL Bluetooth 2.0 9-Axis Gyro Angle Magnetic Sensor, 2026. Available online: https://witmotion-sensor.com/collections/all/products/bluetooth-2-0-9-axis-gyro-angle-magnetic-sensor-bwt901cl (accessed on 12 June 2026).
24. maxon motor. EC 45 flat, Brushless, 30 Watt Datasheet, 2021. Available online: https://www.maxongroup.co.kr/medias/sys_master/root/8882562924574/EN-21-295.pdf (accessed on 12 June 2026).
25. maxon motor. EPOS4 Module/Compact 50/5 Positioning Controller Hardware Reference, 2025. Available online: https://www.maxongroup.co.kr/medias/sys_master/root/9444048273438/EPOS4-Module-Compact-50-5-Hardware-Reference-En.pdf (accessed on 12 June 2026).
26. maxon motor. Encoder MILE 256–2048 CPT, 2 Channels, with Line Driver Datasheet, 2021. Available online: https://www.maxongroup.co.kr/medias/sys_master/root/8883954745374/EN-21-460-461.pdf (accessed on 12 June 2026).
27. Leadshine. iCS-RS1706 Integrated Closed Loop Stepper Motor, 2026. Available online: https://www.leadshine.com/product-detail/iCS-RS1706.html (accessed on 12 June 2026).